Journal of The Electrochemical Society, **156** (9) B1004-B1021 (2009)
0013-4651/2009/156(9)/B1004/18/$25.00 © The Electrochemical Society

Modeling Electrochemical Oxidation of Hydrogen on Ni–YSZ Pattern Anodes

David G. Goodwin,[a,*] Huayang Zhu,[b,*] Andrew M. Colclasure,[b] and Robert J. Kee[b,*,z]

[a]*California Institute of Technology, Pasadena, California 91125, USA*
[b]*Colorado School of Mines, Golden, Colorado 80401, USA*

A computational model is developed to represent the coupled behavior of elementary chemistry, electrochemistry, and transport in the vicinity of solid-oxide fuel cell three-phase boundaries. The model is applied to assist the development and evaluation of H_2 charge-transfer reaction mechanisms for Ni–yttria-stabilized zirconia (YSZ) anodes. Elementary chemistry and surface transport for the Ni and YSZ surfaces are derived from prior literature. Previously published patterned-anode experiments [J. Mizusaki et al., *Solid State Ionics*, **70/71**, 52 (1994)] are used to evaluate alternative electrochemical charge-transfer mechanisms. The results show that a hydrogen-spillover mechanism can explain the Mizusaki polarization measurements over wide ranges of gas-phase composition with both anodic and cathodic biases.
 [DOI: 10.1149/1.3148331]

Manuscript submitted February 2, 2009; revised manuscript received April 6, 2009. Published July 6, 2009.

Establishing elementary charge-transfer reaction pathways is one of the most difficult aspects of understanding the fundamental behavior of solid oxide fuel cells (SOFCs). Most modeling efforts represent charge transfer in terms of activation overpotentials and the Butler–Volmer equation. The objective of the present paper is to develop an elementary representation of the transport, chemistry, and electrochemistry in the vicinity of an anode three-phase boundary (TPB) between gas-phase H_2, a Ni anode, and a yttria-stabilized zirconia (YSZ) electrolyte. The approach is based upon quantitative models and previously reported patterned-anode experiments by Mizusaki et al.[1]

Mizusaki et al.[2] developed model anode structures using thin nickel films on single-crystal YSZ. The nickel films were patterned lithographically into an array of lines. By varying the linewidth and spacing, it was possible to control the TPB length per unit area. Others have followed Mizusaki's lead, and several experimental studies have been reported.[3-7] Nevertheless, Mizusaki's 1994 paper stands as the most complete data set available. The experiments were carefully designed to impose both cathodic and anodic potentials and to systematically vary the H_2 partial pressure while holding H_2O partial pressure constant and vice versa.

In addition to electrochemical charge transfer, the model simultaneously represents the competing processes of surface-diffusive transport and nonfaradaic chemistry on the Ni and YSZ surfaces. The reaction pathways and rates for thermal surface reactions are drawn from independent experimental and theoretical literature. The reaction mechanisms are constructed hierarchically, beginning with the nonfaradaic processes, and then adding charge-transfer reactions at the TPB, without modifying the rates or equilibrium constants for the nonfaradaic reactions. In this way, it is possible to develop robust reaction mechanisms that are applicable over wide ranges of operating conditions.

The model is used to evaluate the validity of two alternative charge-transfer pathways. One is an oxygen-spillover mechanism in which the rate-limiting reaction involves atomic oxygen from the YSZ surface crossing over to the Ni. The other is a hydrogen-spillover mechanism in which the rate-limiting reaction involves an H atom from the Ni surface crossing over to the YSZ. The results show that the hydrogen-spillover mechanism represents the Mizusaki measurements very well, while the oxygen-spillover mechanism cannot represent the entire set of experiments.

Results of the present models are directly applicable to particle-scale reaction-diffusion models such as the one developed by Williford and Chick.[8] Compared to random arrays of particles within ceramic–metallic composites, the well-defined pattern-electrode experimental and modeling framework facilitates the quantitative interpretation of interactions between thermal chemistry, surface transport, and electrochemical charge transfer.

* Electrochemical Society Active Member.
z E-mail: rjkee@mines.edu

Modeling approach.— Compared to traditional fuel-cell models, the approach taken here is quite different. Most fuel-cell models begin by evaluating an equilibrium reversible potential (Nernst potential) based upon gas-phase compositions. Then, various current-dependent overpotentials are subtracted from the reversible potential to determine the operating cell potential. Charge transfer is usually represented in terms of the Butler–Volmer equation and activation overpotentials.

There is essentially no controversy over the global electrochemical oxidation process by which H_2 is oxidized. However, despite over 2 decades of research,[1,3-5,9-13] the elementary reaction steps are still poorly understood. Even the qualitative nature of the charge-transfer process is unresolved. For example, important questions include where water formation occurs (i.e., on the metal, on the oxide, or directly at the TPB), the significance of surface-transport processes, and the influence of nonfaradaic reactions (i.e., heterogeneous surface chemistry). Charge transfer clearly depends upon gas-phase composition in the three-phase regions. Thus, it is important to resolve questions about the influence of fuel-composition variations associated with fuel depletion and transport limitations through porous electrode structures. The answers to these questions are not just of academic interest, but significantly affect the design and optimization of practical fuel cells.

In the present model, all chemical processes (thermal and electrochemical) are written as elementary reversible reactions whose rates are represented through fundamental mass-action kinetics. Microscopic reversibility is assured through thermodynamically consistent properties for all participating species. Open-circuit potential is an outcome of the model, not a starting point. There are many potential benefits associated with the elementary approach. For example, parallel charge-transfer pathways can be represented unambiguously. Representing parallel charge-transfer pathways in terms of a Nernst potential and activation overpotentials requires significant limiting assumptions. For example, if gas-phase H_2 and CO are not in chemical equilibrium, there is no unambiguous way to establish a Nernst potential.

Goodwin proposed the direct incorporation of elementary charge-transfer reaction mechanisms into SOFC models.[14] This proposal followed related efforts in which a set of charge-transfer reactions was reduced to a modified Butler–Volmer form using some simplifying assumptions.[15,16] Bessler and others built upon the approach of incorporating elementary charge-transfer reactions and explored alternative charge-transfer pathways.[17-20]

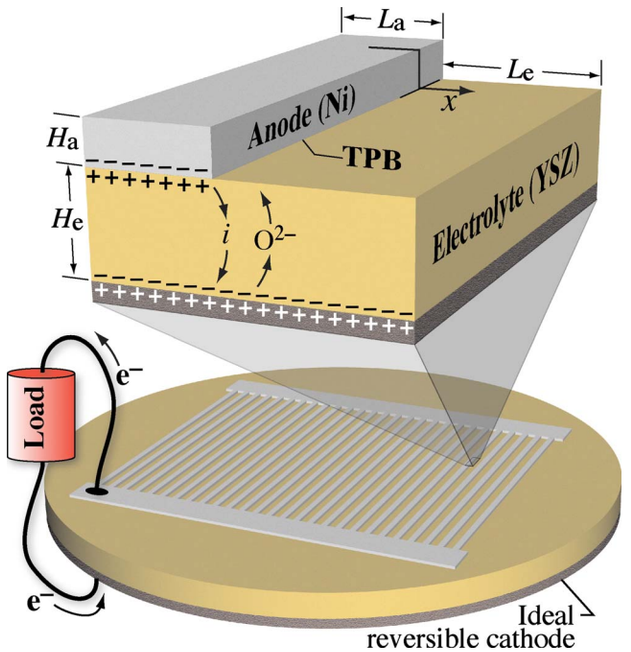

Figure 1. (Color online) Illustration of the pattern anode and the model geometry.

As much as possible, the models presented here build upon independent, published information about thermodynamic properties, thermal chemistry, and surface transport. In other words, parameters associated with these processes are not varied as a means to fit measured electrochemical performance. For each of the alternative elementary charge-transfer reaction pathways, rate expressions (i.e., pre-exponential factors and symmetry factors) are adjusted to achieve the best possible representation of the Mizusaki measurements. The process leads to significant quantitative insight concerning the fundamental charge-transfer chemistry.

This paper focuses on hydrogen as the fuel. However, the approach sets the foundation for extensions to CO and then hydrocarbons. For all hydrocarbon and syngas (H_2 and CO) fuels, hydrogen charge-transfer chemistry is central to fuel-cell performance.

Model Formulation

The patterned-anode configuration consists of a supporting dense electrolyte (YSZ) disk that is patterned with an array of thin, straight, equally spaced metal (Ni) lines on one side. Because the lines are typically a few tens of micrometers wide and the disk diameter is on the order of centimeters, away from the edges of the disk the configuration may be approximated as a periodic array of metal lines. Thus, it was sufficient to simulate only a domain extending from the center of one metal line to the center of the exposed electrolyte adjacent to the line, with symmetry boundary conditions at each end of the domain. As illustrated in Fig. 1, L_a is one-half of the linewidth and L_e is one-half of the exposed electrolyte width. The line thickness is H_a and the electrolyte thickness is denoted as H_e.

The YSZ electrolyte is assumed to be a pure ion conductor, and the metal strips is assumed to be purely electron conductors. Charge carriers in the metal (electrons) cannot cross the interface to the electrolyte nor can the ionic charge carriers in the oxide cross into the metal. Therefore, the metal-oxide interface is purely capacitive, forming a classic double layer. Because the double layer is extremely thin (order of nanometers), it may be represented in the model as a capacitor that is characterized by a specified differential capacitance C_{dl} per unit area.

The overall model is composed of several coupled submodels. As described in the following sections, these include the electrical model, the surface-transport model, and the chemistry model. The coupled model forms a system of one-dimensional reaction-diffusion equations. The transient implementation forms a system of parabolic partial differential equations that is solved via a method-of-lines algorithm. In the steady-state implementation, the system is an ordinary differential equation boundary-value problem that is solved using a modified Newton iteration.

Electrical model.— The electrical model represents the time-dependent electric potential of the anode-side metal strips relative to a reference electrode on the opposite side of the electrolyte disk. The reference electrode is an ideal reversible cathode that is exposed to a constant oxygen partial pressure, p_{O_2}. The model predicts the faradaic current associated with charge transfer at the TPB, which is coupled with the thermal chemistry model. The electrical model also considers the current due to charging or discharging the double layer, given a specified external current.

There is an electric-potential difference $E_a = \phi_a - \phi_{e,a}$ across the anode-electrolyte double layer. The electric potential ϕ_a is the electric potential in the metal electrode, and $\phi_{e,a}$ is the electric potential in the electrolyte immediately outside the double layer. For the low current densities produced in pattern anodes (i.e., $i < 0.1$ mA/cm^2), both ϕ_a and $\phi_{e,a}$ are assumed to be spatially uniform. The charge per unit area stored on the metal side of the double layer is denoted as q_{dl}. On the electrolyte side of the double layer, there is an equal and opposite charge density $-q_{dl}$, which results from the mobile oxygen vacancies entering or leaving the double layer.

Because the domain shown in Fig. 1 has an overall width of $L_e + L_a$, unit depth, and one TPB, the length of the TPB per unit area is $\lambda_{TPB} = 1/(L_e + L_a)$. The faradaic current per unit length of the TPB i_{TPB} (A/cm) is the result of charge-transfer reactions at the TPB regions. These reactions inject electrons into or remove electrons from the metal strip. The gas-phase composition, temperature, and any other factors that affect i_{TPB} are assumed identical at every point on each TPB line; therefore, i_{TPB} is the same everywhere on the TPB line at any instant in time. The faradaic current per unit length i_{TPB} is related to the measurable average faradaic current density (A/cm^2) by $i_F = \lambda_{TPB} i_{TPB}$.

The cathode side of the electrolyte disk is exposed to a constant oxygen partial pressure p_{O_2}. Because the cathode behaves as an ideal reversible electrode, the global oxygen-reduction reaction

$$\tfrac{1}{2}O_2 + V_O + 2e^- \rightleftharpoons O_O^{2-} \quad [1]$$

remains in equilibrium. Here O_O^{2-} and V_O represent the bulk oxygen and the bulk oxygen vacancy. Therefore, the cathode potential relative to the electrolyte potential is fixed at the value

$$\phi_c - \phi_{e,c} = \frac{1}{2F}\left[-\Delta G^\circ + RT\ln\left(\frac{X_{V_O}}{1 - X_{V_O}}\right) + RT\ln(p_{O_2}^{1/2})\right] \quad [2]$$

where ΔG° is the change in standard free energy of Reaction 1 and X_{V_O} is the mole fraction of bulk oxygen vacancies, which is set by the yttrium doping level in YSZ. The electrolyte electric potential just inside the cathode double layer is designated as $\phi_{e,c}$.

The potential difference across the dense electrolyte is given by

$$\phi_{e,c} - \phi_{e,a} = i_F H_e/\sigma \quad [3]$$

where σ is the ionic conductivity of the electrolyte. $\phi_{e,c}$ and $\phi_{e,a}$ are the electrolyte potentials at the cathode- and anode-electrolyte interfaces, respectively. However, for the low currents associated with pattern electrodes, the electrolyte electric potential is assumed spatially uniform. This means that all the spatial variations within the dense electrolyte are negligibly small compared to the electric-potential difference across the double layer between the electrolyte and the electrode.

The charge balance for the patterned metal strip is given as

$$\frac{dq_{\mathrm{dl}}}{dt} = i_{\mathrm{ext}} - i_{\mathrm{F}} \quad [4]$$

Here i_{ext} is the current density per unit area coming from (or supplied to) an external circuit. The external current density is specified as a function of time (galvanostatic control). The faradaic current density i_{F} is computed dynamically by the model. The functional form of i_{ext} is determined by the type of electrochemical experiment being simulated. For example, to compute the open-circuit potential, i_{ext} is set to zero; to compute the steady-state polarization response, i_{ext} is set to a constant positive value for anodic polarization or a constant negative value for cathodic polarization. To simulate impedance spectra, i_{ext} is set to a transient harmonic function proportional to $\sin(\omega t)$.

The faradaic current density per unit TPB length i_{TPB} depends upon the electric-potential difference across the double layer at the anode TPB ($E_{\mathrm{a}} = \phi_{\mathrm{a}} - \phi_{\mathrm{e,a}}$) and also upon the activities of surface species that participate in the charge-transfer process. Therefore, a set of reaction-diffusion equations must be coupled with Eq. 4 to close the system of equations. These equations represent the transport of adsorbates as well as nonfaradaic reactions on the metal and electrolyte surfaces.

In general, ohmic potential variations within the dense electrolyte should also be considered in evaluating E_{a}. However, it is possible to correct for ohmic potential drops experimentally by using current-interruption techniques. Because this was done in the Mizusaki's experiments, no explicit consideration of ohmic potential drops is required in the model. Even if current interruption does not completely correct for all ohmic losses, their magnitude within the electrolyte layer is small for the very low current densities in pattern anodes. At a current density of 0.1 mA/cm^2, assuming an electrolyte thickness of 1 mm and an ion conductivity of 0.02 S/cm, the ohmic potential drop across the electrolyte is only 0.5 mV, which is quite small compared to an activation polarization of approximately 200 mV as measured by Mizusaki et al.[1]

Reaction-diffusion equations.— The faradaic current i_{TPB} is the result of charge-transfer reactions at the TPB. The rates of these reactions depend upon the activities of the reactant and product species near the interface. Usually, these are surface species, not gas-phase species, and their activities depend upon a complex interplay between surface reaction and transport processes.

Because the patterned-anode TPB is a long straight line, the species transport by surface diffusion is one dimensional and perpendicular to the TPB line. As illustrated in Fig. 1, the spatial coordinate x is measured from the TPB line with the metal surface to the left of the interface ($x < 0$) and the electrolyte surface to the right ($x > 0$). On the metal strip, the x coordinate follows the surface contour. The results show that variations in metal-surface species coverages are confined to the region very close to the TPB. Thus, the one-dimensional representation of the metal pattern is reasonable.

The metal surface is assumed to have a fixed number of surface-adsorption sites per unit area Γ, and all sites are equivalent. Species may be adsorbed on the metal surface, and the species activities are assumed to be proportional to the fractional surface coverages θ_k. It is convenient to regard every possible state of a surface site as a "surface species" with associated thermodynamic properties. Thus, an unfilled surface site is also considered as a species.

Adsorbed species may be mobile on the surface via hopping mechanisms to available neighboring sites. If D_k (cm^2/s) is the surface diffusion coefficient of adsorbate k in the low-coverage limit, then the surface flux of adsorbate k may be written as

$$J_k = - D_k \frac{\partial [X_k]}{\partial x} \quad [5]$$

For each surface adsorbate, the surface concentration $[X_k](x,t)$ is determined from the solution of

$$\frac{\partial [X_k]}{\partial t} = D_k \frac{\partial^2 [X_k]}{\partial x^2} + \dot{s}_k \quad [6]$$

The concentrations are simply related to the coverages via the available site density as $[X_k] = \Gamma \theta_k$. The net production rates due to nonfaradaic surface reactions are represented as $\dot{s}_k$ (mol/cm^2 s). Equation 6 applies to both the metal and the electrolyte surfaces, although the adsorbate species, diffusion coefficients, and reaction mechanisms are generally different on the two surfaces.

The solution to Eq. 6 depends upon boundary conditions. Consider first the metal anode surface. At the symmetry plane

$$\frac{\partial [X_k]}{\partial x} = 0, \quad x = - L_{\mathrm{a}} - H_{\mathrm{a}} \quad [7]$$

At the TPB

$$D_k \frac{\partial [X_k]}{\partial x} = \dot{c}_k, \quad x = 0 \quad [8]$$

The term $\dot{c}_k$ is the net production rate of species k due to charge-transfer reactions at the TPB. The value of $\dot{c}_k$ is nonzero for only the surface species that participate directly in the charge-transfer reactions. The symmetry boundary condition for the electrolyte surface is

$$\frac{\partial [X_k]}{\partial x} = 0, \quad x = L_{\mathrm{e}} \quad [9]$$

As with the metal surface, the TPB condition for the electrolyte surface is written as

$$D_k \frac{\partial [X_k]}{\partial x} = - \dot{c}_k, \quad x = 0 \quad [10]$$

The electrolyte-surface species production rates via charge transfer are equal in magnitude but opposite in sign to the rate for the metal surface.

Surface thermodynamics.— The principle of detailed balance requires that the forward and reverse rates of every elementary reaction balance individually whenever the conditions of thermodynamic equilibrium are met. This is a much stronger statement than one that simply requires the net production rate of each species to be zero at equilibrium. The state of thermodynamic equilibrium is one in which the Gibbs free energy is minimal with respect to the reaction coordinate for every conceivable balanced reaction.

Expressions for the chemical potentials μ_k of surface, bulk, and gaseous species are needed to evaluate equilibrium conditions. The chemical potentials may be represented as

$$\mu_k = \mu_k^{\circ} + RT \ln a_k \quad [11]$$

where a_k is the activity of species k, and μ_k° is the standard-state chemical potential, or chemical potential at unit activity. The activity of a gas-phase species is evaluated as its molar concentration (i.e., mol/cm^3), the activity of a surface species is evaluated as the surface molar concentration (i.e., mol/cm^2), and the activity of a bulk species is evaluated as its bulk-phase mole fraction.

Thermal and charge-transfer reactions.— To evaluate Eq. 6, 8, and 10, expressions are required for the surface-species production rates by surface reaction (i.e., $\dot{s}_k$) and the electrochemical charge-transfer rates at the TPB (i.e., $\dot{c}_k$). In both cases, care must be taken that the net production rates vanish when the conditions for thermodynamic equilibrium are satisfied. This in turn requires that rate expressions are thermodynamically consistent. Constraining the rate expressions is somewhat different for the thermal (nonfaradaic) surface reactions and the charge-transfer reactions. Because the thermal surface chemistry is well documented,[21,22] the formulation is not discussed further here.

Charge-transfer reactions.— Species production rates for charge-transfer reactions at the TPB are written as

$$\dot{c}_k = \sum_{i=1}^{I} \nu_{ki} q_i \quad [12]$$

where ν_{ki} are stoichiometric coefficients for species k participating in reaction i, q_i is the rate of progress for the ith reaction, and there is a total of I reactions. For a Ni–YSZ interface, charge-transfer reactions occur across the TPB interface, not on a single surface (the situation is different for mixed-conducting materials). Therefore the units of q_i are mol/cm s, where the length scale is the length of the TPB. Of particular interest is the production rate of electrons at the TPB given by

$$\dot{c}_e = \sum_{i=1}^{I} \nu_{ei} q_i \quad [13]$$

where $\nu_{ei} = +1$ for reactions written in the anodic direction, and -1 for reactions written in the cathodic direction. Although it is common to write global one-step reactions that involve the transfer of two or more electrons [e.g., $O_2(g) + 4e^- \rightleftharpoons 2O^{2-}$], these are global reactions that may be decomposed into a set of elementary reactions. All known elementary reactions transfer only a single electron.

Consider a generic charge-transfer reaction written in the anodic direction (i.e., producing electrons)

$$A + B \rightleftharpoons C + D + e^- \quad [14]$$

where net rate of progress may be written as the difference between anodic and cathodic rates

$$q = q_a - q_c \quad [15]$$

In addition to temperature, the anodic and cathodic rates also depend upon the electric-potential difference across the double layer $E_a = \phi_a - \phi_{e,a}$ as

$$q_a = k_a(T) a_A a_B \exp\left(\frac{\beta_a F E_a}{RT}\right) \quad [16]$$

and

$$q_c = k_c(T) a_C a_D \exp\left(\frac{-\beta_c F E_a}{RT}\right) \quad [17]$$

The thermal contributions k_a and k_c are usually written in Arrhenius form. For elementary reactions, the symmetry parameters β satisfy $0 < \beta < 1$. Further, the anodic and cathodic symmetry parameters are constrained to satisfy $\beta_a + \beta_c = 1$. In global reactions, symmetry parameters are also relevant but usually called α not β. For global reactions there are no specific constraints on the values of α.

The forward (anodic) and reverse (cathodic) rate constants must still satisfy microscopic reversibility. That is

$$\frac{k_a}{k_c} = K_{eq} = \exp\frac{-\Delta G^\circ}{RT} \quad [18]$$

where ΔG° is the standard-state free-energy change of the reaction. The electron does not contribute to ΔG° because the chemical potential of an electron at the Fermi level of a metal is zero.

For the generic charge-transfer reaction, Eq. 16 and 17 result in the Nernst equation, expressing the equilibrium electric-potential difference at the anode as

$$E_a^{eq} = \frac{1}{F}\left[\Delta G^\circ + RT \ln\left(\frac{a_C a_D}{a_A a_B}\right)\right] \quad [19]$$

If there are multiple charge-transfer reactions, at equilibrium every charge-transfer reaction must be equilibrated simultaneously with the same value of E_a^{eq}; in this case, the set of Nernst equations define constraints that the equilibrium species activities must satisfy. However, if for any reason the species activities were not in equilibrium, then it is not possible to unambiguously define a Nernst potential, especially with parallel charge-transfer pathways.

In the present model, the rates of all charge-transfer reactions are evaluated from Eq. 16-18. The faradaic current is then computed from

$$i_{TPB} = F \sum_i (q_{i,a} - q_{i,c}) \quad [20]$$

where the summation runs over all charge-transfer reactions.

Most SOFC modeling studies use Butler–Volmer expressions to compute the faradaic current instead of the elementary mass-action formulation used here. The activation overpotential, which is needed in the Butler–Volmer equation, is defined in terms of E_a^{eq}, which is computed from Eq. 19 using the actual activities that exist under polarization. The equilibrium electric-potential difference is often different from the open-circuit anode potential. For example, the species activities at the TPB interface may depend upon the current density as a result of slow surface transport rates to or from the TPB. Only if the charge-transfer reaction is rate limiting, such that the activities are established by much faster nonfaradaic processes (e.g., rapid adsorption–desorption equilibrium with gaseous species), can the Butler–Volmer equation be used with an overpotential referenced to open circuit.

If multiple charge-transfer pathways are active, then away from equilibrium, the value of E_a^{eq} as computed from Eq. 19 has different values for each reaction, resulting in significant complications in using the Butler–Volmer formulation. By contrast, the physical anode potential E_a has a single, unambiguous value, independent of how many charge-transfer pathways are operative. Moreover, it is straightforward to use Eq. 16 and 17 directly. For models such as the present one, in which the anode potential, species activities, and current density are all computed self-consistently, the Butler–Volmer form offers no substantial advantages compared to the elementary mass-action form. More importantly, representing reactions in the mass-action form does not suffer from restrictions that are inherent in the Butler–Volmer form.

Transport and Chemistry on Ni

The previous section develops and describes the mass-action kinetics in general terms. In this section, the development is specific to the Ni phase within the Ni–YSZ anode.

Heterogeneous chemistry on Ni.— The interactions of hydrogen, oxygen, and steam on nickel surfaces are widely studied. The surface reactions and their rates are adopted from Deutschmann and co-workers,[23,24] where the hydrogen oxidation forms part of a larger reaction mechanism for methane reforming on a nickel surface. Table I lists the five reactions that involve noncarbonaceous species, giving the forward rate parameters in Arrhenius form. In these reactions, (Ni) represents an empty adsorption site on the nickel surface, H(Ni) is an adsorbed H atom, and O(Ni) and OH(Ni) represent adsorbed oxygen and hydroxyl, respectively. Table I also provides the standard-state enthalpy and free-energy changes for each reaction at 700°C. A potential oxygen adsorption–desorption reaction is neglected. Because oxygen bonds strongly to the Ni surface, O(Ni) will not desorb as O_2, especially when H(Ni) is available such that H_2O(Ni) can be formed. Further, under ordinary SOFC anode operating conditions, where the gas-phase O_2 partial pressure is extremely low, oxygen adsorption is unimportant.

To maintain strict thermodynamic consistency, the reverse rates in the present paper are evaluated from the thermodynamic properties stated in Table II. Therefore, the reverse rates given by Janardhanan and Deutschmann[23] are not used. However, the resulting changes to the reverse rate coefficient values are relatively small and well within the uncertainty in these values.

Surface diffusion on Ni.— Adsorbed hydrogen on the nickel surface is mobile, and Mogensen and Skaarup[25] provided an expression for the diffusion coefficient (cm^2/s) of H on Ni as

Table I. Heterogeneous reaction mechanism on a nickel surface. ΔH° and ΔG° are evaluated at 700°C. The available site density is $\Gamma = 1.7 \times 10^{-9}$ mol/cm^2.

Reaction	A[a] or γ_0 (mol,cm,s)	E (kJ/mol)	ΔH° (kJ/mol)	ΔG° (kJ/mol)
$H_2(g) + 2(Ni) \rightleftharpoons 2H(Ni)$ [21]	0.01[b]	0.0	85.36	−1.62
$H_2O(g) + (Ni) \rightleftharpoons H_2O(Ni)$ [22]	0.10[b]	0.0	−64.39	41.47
$H(Ni) + O(Ni) \rightleftharpoons OH(Ni) + (Ni)$ [23]	5.0×10^{22}	97.9	61.74	34.83
$H(Ni) + OH(Ni) \rightleftharpoons H_2O(Ni) + (Ni)$ [24]	3.0×10^{20}	42.7	−49.17	−32.83
$2OH(Ni) \rightleftharpoons H_2O(Ni) + O(Ni)$ [25]	3.0×10^{21}	100.0	−110.91	−67.66

[a] The forward rate coefficients are given in Arrhenius form as $k = A \exp(-E/RT)$.
[b] Sticking coefficient in the form of $\gamma = \gamma_0 \exp(-E/RT)$. The sticking coefficient is dimensionless.

$$D_H = 2.5 \times 10^{-3} \exp(-E_H/RT) \quad [26]$$

with $E_H = 14.65$ kJ/mol. At 700°C, the value of D_H is 4×10^{-4} cm^2/s.

The other adsorbed surface species are expected to have relatively limited mobility at 700°C. Nevertheless, at this temperature, the nickel atoms themselves are mobile to some extent. The nickel self-diffusion coefficient D_{Ni} is given as[25]

$$D_{Ni} = 1.4 \times 10^{-2} \exp(-E_{Ni}/RT) \quad [27]$$

with $E_{Ni} = 93.2$ kJ/mol. At 700°C, this results in $D_{Ni} = 1.4 \times 10^{-7}$ cm^2/s. It is unlikely that adsorbates on nickel could be less mobile than the underlying nickel atoms. Thus, as a lower limit, all adsorbates other than hydrogen are assumed to have diffusion coefficients equal to the nickel self-diffusion coefficient.

Chemistry and transport on Ni.— Even before considering electrochemistry directly, much can be inferred about potential rate-limiting charge-transfer processes through the analysis of transport and chemistry on the Ni surface. Previous studies have proposed that the rate-limiting process may not be the charge-transfer step but rather a nonfaradaic reaction on the nickel surface.[26] For the narrow purpose of studying reaction and diffusion on the Ni surface, charge-transfer reactions at the TPB can be assumed to behave simply as sources or sinks of species on the Ni surface. For a given anodic current density i_F, there must be either a flux of surface hydrogen toward the TPB or a flux of surface oxygen from the TPB, depending on the charge-transfer process. To investigate the rate limitations, it is informative to solve reaction-diffusion equations on the nickel surface using specified surface-species fluxes at the TPB. The magnitudes of these boundary fluxes correspond to the anodic (or cathodic) current at the TPB. Two cases are considered here: One in which a source of O(Ni) is imposed at the TPB, and the other in which a sink of H(Ni) is imposed at the TPB. Far from the TPB, zero-flux boundary conditions are imposed.

Table II. Standard-state thermodynamic properties for species at 700°C.

Species	H° (kJ/mol)	S° (J/mol K)
$H_2(g)$	19.9	165.3
$H_2O(g)$	−217.8	231.5
$O_2(g)$	21.8	242.3
(Ni)	0.0	0.0
H(Ni)	−32.7	39.6
$H_2O(Ni)$	−281.6	122.5
OH(Ni)	−199.7	99.6
O(Ni)	−228.7	32.4

Mizusaki et al.[1] reported pattern-anode data with TPB currents of $i_{TPB} = i_F/\lambda_{TPB} = 0.06$ mA/m (6×10^{-4} mA/cm). Assuming a possible global reaction at the TPB as

$$H_2(g) + O(Ni) \rightarrow H_2O(g) + (Ni) \quad [28]$$

the current would correspond to a flux of surface oxygen O(Ni) of $i_F/2F\lambda_{TPB} = 3.11 \times 10^{-12}$ mol/cm s away from the TPB. If H(Ni) is responsible for the charge transfer, a surface-hydrogen H(Ni) flux of $i_F/F\lambda_{TPB} = 6.22 \times 10^{-12}$ mol/cm s toward the TPB would be required.

Figures 2 and 3 show two sets of predictions of surface-coverage and reaction-rate profiles. In both cases, the gas phase above the surface is fixed at 97% H_2 and 3% H_2O. The diffusion coefficients and heterogeneous reactions are those discussed in the previous sections. At distances greater than about 5 nm from the TPB, the coverages and reaction rates for both cases are essentially independent of position. The reason for this behavior is that the coverages far from the TPB are established by equilibrium between the surface and the gas-phase composition, and not affected by charge-transfer rates at the TPB.

For imposed H(Ni) flux (Fig. 2), the coverages remain nearly uniform everywhere on the Ni surface. This behavior is the result of the surface chemistry being fast relative to the diffusion rates and that only a small concentration gradient is needed to supply the required hydrogen flux to the TPB. The surface reactions, primarily reaction 21, produce the needed H(Ni) by dissociative adsorption of gas-phase H_2.

For imposed O(Ni) flux, the behavior is qualitatively different from that associated with the imposed H(Ni) flux. As illustrated in Fig. 3, the coverages of O(Ni) and OH(Ni) are elevated within 5 nm from the TPB but approach their equilibrium values beyond 5 nm. This is the result of the relatively slow transport of surface oxygen away from the TPB, causing a buildup in O(Ni) near the TPB. The OH(Ni) coverage tracks that of O(Ni) because its coverage is set by the balance between production of OH(Ni) by reaction of O(Ni) and H(Ni) and consumption of OH(Ni) by reaction with H(Ni). Although the O(Ni) results show a small degree of transport dependence, it is not sufficient to significantly limit the achievable current. The elevated coverage of O(Ni) remains less than 1%, and the fraction of open surface sites is essentially unaffected. Thus, the O(Ni) transport is not likely to offer a significant rate limitation to the charge transfer.

The present analysis does not include the global reaction proposed by Mizusaki et al.[1] (i.e., Reaction 28). Although the direct reaction of a gaseous hydrogen molecule with surface oxygen to produce H_2O would likely be slow (if it proceeds at all), the com-

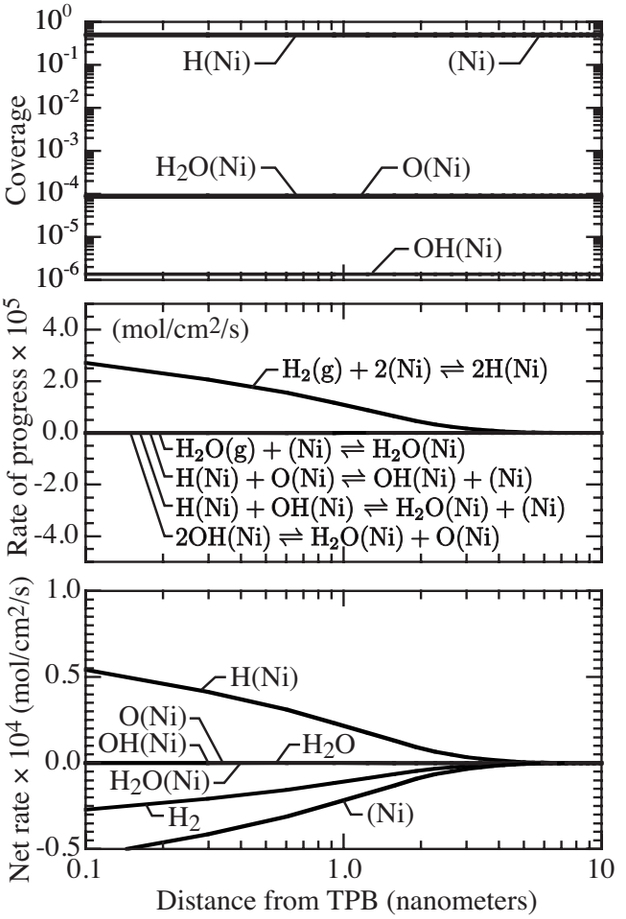

Figure 2. Surface coverages, surface-reaction rates of progress, and net production rates by surface reactions on the Ni surface under anodic polarization by imposing the H(Ni) flux toward the TPB such that i_F/λ_{TPB} = 0.06 mA/m.

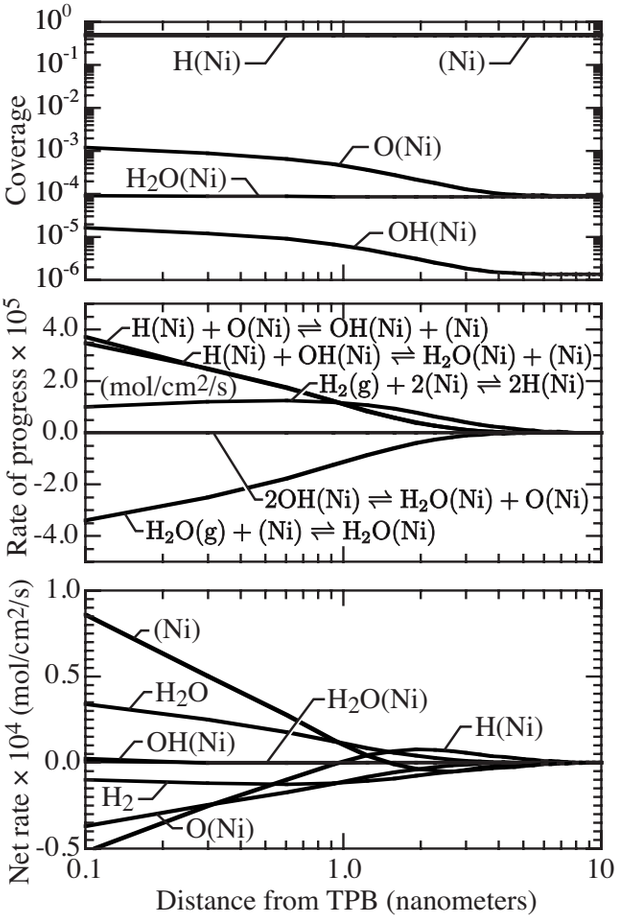

Figure 3. Surface coverages, surface-reaction rates of progress, and net production rates by surface reactions on the Ni surface under anodic polarization by imposing the O(Ni) flux away from the TPB such that i_F/λ_{TPB} = 0.06 mA/m.

petition with the much faster water-formation pathway represented by reactions 21-25 would render any such slow pathway to be unimportant.

Chemistry and Thermodynamic Properties on YSZ

YSZ bulk phase.— In the bulk YSZ, oxygen lattice sites may be occupied either by an oxygen ion or they may be vacant. The occupied site is denoted as O_O^{2-} and the empty site by V_O. For charge bookkeeping, it is convenient to associate a −2 charge with the oxygen ions and to regard the vacancies as uncharged. This differs from the Kröger–Vink convention, in which the charge is defined relative to the value for the defect-free crystal. Thus, in a Kröger–Vink notation a lattice oxygen ion is regarded as uncharged, and an oxygen vacancy has a charge of +2. The present choice is made to simplify writing charge-balanced reactions involving both bulk species and surface species. The crystal is assumed to be charge neutral with positively charged cations providing the compensating charge. The vacancy mole fraction is fixed at the value that results in an uncharged crystal, which is a function of the yttrium doping level.

To determine the standard-state chemical potential of the bulk oxygen ion, consider the global oxygen-reduction reaction at the reference electrode on the cathode side (i.e., Reaction 1). At equilibrium

$$\frac{1 - X_{V_O}}{p_{O_2}^{1/2} X_{V_O}} = \exp\left(\frac{-\Delta G^\circ}{RT}\right)\exp\left(\frac{-2FE_c}{RT}\right) \quad [29]$$

where X_{V_O} is the bulk oxygen vacancy fraction and $(1 - X_{V_O})$ is the O_O^{2-} fraction. The electric-potential difference across the double layer at the reference electrode is $E_c = \phi_c - \phi_{e,c}$. The bulk vacancy fraction is set by the yttrium doping level as $X_{V_O} = 0.0374$ for 8 mol % Y_2O_3 in ZrO_2.[27] The standard-state free-energy change for the reaction is

$$\Delta G^\circ = \mu^\circ_{O_O^{2-}} - \tfrac{1}{2}\mu^\circ_{O_2(g)} - \mu^\circ_{V_O} \quad [30]$$

By convention, the chemical potential of the vacancy is set to zero. The ion chemical potential is then

$$\mu^\circ_{O_O^{2-}} = -2FE_c + \frac{1}{2}(\mu^\circ_{O_2(g)} + RT\ln p_{O_2}) - RT\ln\left(\frac{1 - X_{V_O}}{X_{V_O}}\right) \quad [31]$$

The absolute cathode-electrolyte electric-potential difference E_c cannot be measured by conventional means because it cancels out of any measurement of the difference in electric potential between two metal electrodes. Therefore, E_c may be set arbitrarily by selecting an appropriate value for $\mu^\circ_{O_O^{2-}}$ (bulk-phase oxygen-ion chemical potential). Here the electric-potential difference across the cathode double layer is fixed as E_c = 0.5 V. This choice is purely for conceptual

Table III. Thermodynamic properties of species on YSZ at 700°C.

Species	H° (kJ/mol)	s° (J/mol K)
V_O	0.0	0.0
O_O^{2-}	−85.6	148.4
(χ)	0.0	0.0
$O^{2-}(\chi)$	−85.6	139.6
$O^{-}(\chi)$	−85.6	139.6
$OH^{-}(\chi)$	−173.8	124.5
(Zr)	0.0	0.0
OH^{-}(Zr)	−208.8	124.5
H^{-}(Zr)	90.3	37.0

simplicity so that the electrolyte potential lies between the anode and cathode potentials at open circuit. Any other choice could be made without affecting any measurable results. The gas-phase oxygen partial pressure was reported by Mizusaki as $p_{O_2} = 1$ atm. However, a different value of p_{O_2} could be used, resulting in a shift of $\mu^\circ_{O_O^{2-}}$. As with the assumption for E_c, all derivative thermodynamic properties would be shifted accordingly. Insofar as all the properties are self-consistent, only the differences in chemical potentials are important.

Beginning with Eq. 31 and noting that $\mu_k^\circ = H_k^\circ - TS_k^\circ$, it follows that

$$\mu^\circ_{O_O^{2-}} = -2FE_c + \frac{1}{2}H^\circ_{O_2(g)} - T\left[\frac{1}{2}S^\circ_{O_2(g)} - \frac{R}{2}\ln p_{O_2(g)} + R\ln\left(\frac{1-X_{V_O}}{X_{V_O}}\right)\right] \quad [32]$$

In this form, assuming that $E_c = 0.5$ V, $p_{O_2} = 1$ atm, and the O_2(g) properties are given in Table II, the properties for the bulk ion are evaluated as

$$H^\circ_{O_O^{2-}} = -2FE_c + \tfrac{1}{2}H^\circ_{O_2(g)} = -85.6 \text{ kJ/mol} \quad [33]$$

$$S^\circ_{O_O^{2-}} = \frac{1}{2}S^\circ_{O_2(g)} + R\ln\left(\frac{1-X_{V_O}}{X_{V_O}}\right) = 148.4 \text{ kJ/mol} \quad [34]$$

Table III lists thermodynamic properties for the bulk oxygen ion and surface species, which are discussed below. All the values in Table III are relative to the assumptions concerning the bulk ion.

YSZ surface phase.— The experiments of Mizusaki et al. were carried out using single-crystal YSZ electrolytes with (100) surface orientation.[1] As-polished YSZ (100) surfaces can contain a rich variety of nanometer-scale surface morphological features (etch pits, adatoms, steps, kinks, etc.),[28] depending upon how the surface is prepared and the extent to which it is annealed. The reactivity of the surface may be affected by the surface morphology because some sites (e.g., steps or kinks) may be more conducive to bonding adsorbed species than others (e.g., flat terrace sites). Attempting to model the surface at this high level of resolution, however, would be virtually impossible, given the current incomplete knowledge of the atomic-level structure and reactivity of the YSZ surface.

For the present study, a relatively simple model of the YSZ surface is adopted. The surface is assumed to be the (1 × 1) reconstruction seen in high resolution medium-energy ion scattering studies from YSZ (100),[29] in which oxygen ions sit above the centers of the squares defined by the topmost cation layer. This surface reconstruction has equal numbers of surface oxygen and zirconium (or yttrium) atoms and is uncharged. Compared to the bulklike, oxygen-terminated surface, which would have a negative charge, this reconstruction has half of the oxygen ions removed.

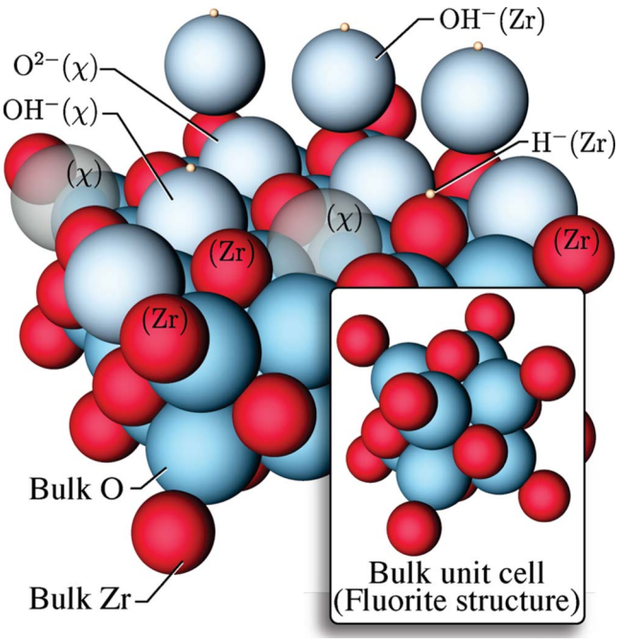

Figure 4. (Color online) Atomic structure of the YSZ surface and surface species that participate in thermal and electrochemical reactions.

Figure 4 illustrates the structure of the YSZ surface and identifies the meanings of the species names. A mobile oxygen ion in the bulk YSZ is designated as O_O^{2-}. A vacancy in the bulk is designated V_O. The reaction chemistry uses two types of surface sites, identified as (Zr) and (χ) sites. An open zirconium site (Zr) represents a surface-level zirconium atom onto which nothing is adsorbed. A hydrogen adsorbed on a surface zirconium is represented as H^{-}(Zr). A hydroxyl adsorbed on a surface zirconium is represented as OH^{-}(Zr).

Based upon the findings of Nishimura et al.,[29] who used high resolution ion scattering to characterize the structure of YSZ (001) surfaces, the (χ) sites have a somewhat different meaning than the (Zr) sites have. To maintain charge neutrality the surface reconstructs with oxygen atoms centered between four zirconium atoms and raised slightly above the plane of the Zr. Nishimura et al. called this the rumpled face. The position of the surface oxygen is quite different from the position of oxygen in the bulk YSZ. In the bulk fluorite structure (see inset of Fig. 4) oxygen atoms are positioned above oxygen atoms and zirconium atoms are positioned above zirconium atoms. In the reconstructed surface the surface oxygens are positioned above lower level zirconium atoms. The meaning of an open (χ) site is defined to be the position that a surface oxygen would occupy if it were present. Figure 4 illustrates the open (χ) sites as transparent oxygen atoms. An oxygen atom that occupies a (χ) site is designated as $O^{2-}(\chi)$. A hydroxyl that occupies a (χ) site is designated as $OH^{-}(\chi)$.

There are 7.57×10^{14} sites/cm^2 for both (χ) and (Zr) with a total site density of 1.51×10^{15} cm^{-2} (i.e., 2.5×10^{-9} mol/cm^2). The surface is assumed to be clean with all sites available to participate in adsorption–desorption reactions. Measurements of impurity levels on the surface of as-received, commercial, single-crystal YSZ by Hansen et al.[30] showed only trace amounts ($< 1\ \%$) of silicon on the surface; the major contaminant seen was carbon, which presumably would not remain at SOFC temperatures.

Surface vacancy fraction.— An important experimental observation that must be modeled is that a greater fraction of the surface sites is

empty than the bulk vacancy fraction.[29] This is likely due to enrichment of yttrium at the surface.[31] Because at SOFC operating temperatures the vacancies are mobile, the surface and bulk vacancies are in dynamic equilibrium. Therefore, the surface and bulk vacancy fractions are related by the equilibrium of the reaction

$$O_O^{2-} + (\chi) \rightleftharpoons O^{2-}(\chi) + V_O \quad [35]$$

The nomenclature here indicates that an oxygen ion from the bulk O_O^{2-} moves to an open surface site (χ) and creates a bulk vacancy. The enhancement in the surface-vacancy fraction may be reproduced by slightly destabilizing the surface oxygen ion relative to the bulk oxygen ion. The equilibrium condition for Reaction 35 may be expressed as

$$\ln\left[\frac{(1-\theta_{(\chi)})X_{V_O}}{(1-X_{V_O})\theta_{(\chi)}}\right] = -\frac{\Delta G_{35}^{\circ}}{RT} \quad [36]$$

Using the values $X_{V_O} = 0.0374$ and $\theta_{(\chi)} = 0.1$ results in $\Delta G_{35}^{\circ}/RT = 1.06$.

Water chemisorption.— Water-vapor chemisorption occurs by bonding to a cation site and transferring a proton to a nearby oxygen site[32]

$$H_2O(g) + (Zr) + O^{2-}(\chi) \rightleftharpoons OH^-(Zr) + OH^-(\chi) \quad [37]$$

With the transfer of the proton to the surface oxygen, the surface potential-energy landscape changes such that it is energetically favorable for the hydroxyl ion to move to a position over a cation, opening a surface oxygen site. This process may be expressed as

$$OH^-(\chi) + (Zr) \rightleftharpoons OH^-(Zr) + (\chi) \quad [38]$$

Because the hydroxyl group on the oxygen site is only a reaction intermediate and not a stable product, its surface coverage is expected to very small. In the model, this can be accomplished by making Reaction 38 fast so that it stays near equilibrium and by choosing the thermodynamic parameters for $OH^-(\chi)$ such that $\mu_{OH^-(\chi)}^{\circ} - \mu_{OH^-(Zr)}^{\circ} \gg RT$, which is 8 kJ/mol at 700°C. This will shift the equilibrium of Reaction 38 toward the products, maintaining the coverage of $OH^-(\chi)$ at a very low level. As long as $H_{OH^-(\chi)}^{\circ} - H_{OH^-(Zr)}^{\circ} \gg RT$, its precise value is unimportant. Here a difference of 35 kJ/mol is used.

The values of $H_{OH^-(Zr)}^{\circ}$ and $S_{OH^-(Zr)}^{\circ}$ were established to fit thermogravimetric measurements by Raz et al.[32] of water-vapor chemisorption on YSZ powder. After correcting for the presence of physisorbed water layers at low temperature, Raz et al. reported that their measured chemisorption data for temperatures up to 700°C can be fitted to

$$\theta_{OH} = \frac{1}{2}\left[\frac{1}{1+(p_{H_2O}K_0)^{-1}e^{-E_1/RT}} + \frac{1}{1+(p_{H_2O}K_0)^{-1}e^{-E_2/RT}}\right] \quad [39]$$

with $E_1 = 94 \pm 19$ kJ/mol and $E_2 = 70 \pm 14$ kJ/mol. Raz et al.[32] did not report the value of K_0, but their data are consistent with a coverage of approximately 50% at 600°C, which implies that $K_0 \approx 4.5 \times 10^{-9}$ Pa^{-1}.

To fit the present model to the data of Raz et al. the transient equations for coverage of the YSZ surface were solved for fixed temperatures and a gas composition of 3% H_2O in oxygen until achieving equilibrium. This process was repeated for a range of temperatures from 200 to 1400 K. The resulting equilibrium coverage of $OH^-(Zr)$ as a function of T was compared to Eq. 39, and the process repeated, varying $H_{OH^-(Zr)}^{\circ}$ and $S_{OH^-(Zr)}^{\circ}$ until an optimal fit was achieved. The best-fit values are $H_{OH^-(Zr)}^{\circ} = -208.8$ kJ/mol and $S_{OH^-(Zr)}^{\circ} = 124.5$ J/mol K, both relative to the empty cation site. The resulting enthalpy of adsorption for the overall adsorption Reactions 37 and 38

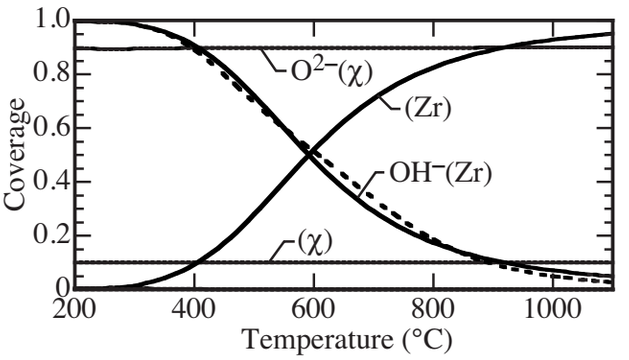

Figure 5. Computed surface species coverages on YSZ as functions of the temperature for an ambient of 97% O_2 and 3% H_2O at 1 atm. The experimental curve (dashed line) is from Raz et al.[32]

$$H_2O(g) + 2(Zr) + O^{2-}(\chi) \rightarrow 2OH^-(Zr) + (\chi) \quad [40]$$

is −115 kJ/mol at 700°C.

Figure 5 compares the computed equilibrium coverage of $OH^-(Zr)$ for a temperature range from 200 to 1100°C with the experimental measurements by Raz et al.[32] As illustrated in Fig. 5, the proposed surface-reaction mechanism matches the experimental observations well. Figure 5 also shows the computed site fractions for all the surface species on both χ and Zr sites. Because Reaction 35 for the exchange of surface and bulk oxygen is fast, the site fractions for the surface species on the χ sites change very little over this temperature range. However, as the temperature increases, the site fraction of $OH^-(Zr)$ drops, which increases the fraction of open Zr sites.

Hydrogen chemisorption.— Hydrogen chemisorption occurs by transferring a proton to an oxygen site and forming a hydride on the cation site[33]

$$H_2(g) + (Zr) + O^{2-}(\chi) \rightleftharpoons H^-(Zr) + OH^-(\chi) \quad [41]$$

As with water chemisorption, $OH^-(\chi)$ is converted rapidly to $OH^-(Zr)$ by Reaction 38. The thermodynamic properties of the hydride species were determined by requiring that the enthalpy of adsorption for Reaction 41 is −17.8 kJ/mol at low temperature, which is the value calculated for dissociative adsorption of molecular hydrogen on tetragonal zirconia by Hofmann et al.[34] The hydride species entropy is 37 J/mol K, which is similar to the entropy of adsorbed hydrogen on Ni. Although there is significant uncertainty in the properties of the hydride species, the uncertainty has very little impact on overall charge-transfer behavior because of the very low coverages. For typical fuel-cell behavior Reaction 41 could be eliminated from the mechanism with essentially no change in the predictive capability.

Figure 6 shows the computed equilibrium surface-species coverages on YSZ as functions of steam partial pressure in gas-phase mixtures of H_2–H_2O at atmospheric pressure and temperatures of 600, 700, and 800°C. As the steam partial pressure increases, H_2O is increasingly adsorbed on the YSZ surface to form $OH^-(Zr)$ species on the Zr sites, and the site fractions of both $H^-(Zr)$ and (Zr) on the Zr sites drop. For H_2O partial pressures that are present in typical SOFC operation (i.e., greater than 3%), the $H^-(Zr)$ coverage is less than around 10^{-3}. On the χ sites, the site fractions of $OH^-(\chi)$ increase as the steam partial pressure increases. However, the coverage of $OH^-(\chi)$ is relatively small, and the open oxygen site fractions (χ) remain essentially unchanged.

Reaction rates.— The results shown in Fig. 5 and 6 are equilibrium predictions, which depend only upon the species thermochemistry, not on the reaction rates. The next task is to assign forward rates for the YSZ surface Reactions 35, 37, 38, and 41. Table IV lists rates for the reaction mechanism used to describe the YSZ surface chemistry.

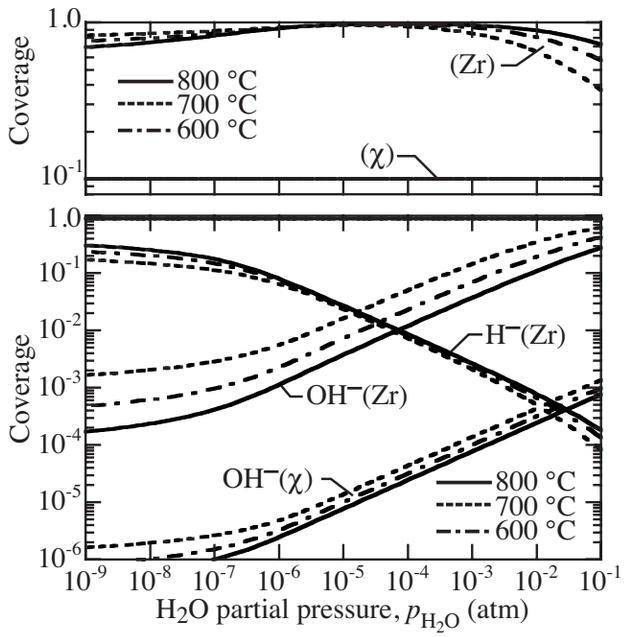

Figure 6. Computed equilibrium surface species coverages on YSZ as functions of the partial pressure of steam for H_2–H_2O gas mixtures at atmospheric pressure and temperatures of 600, 700, and 800°C.

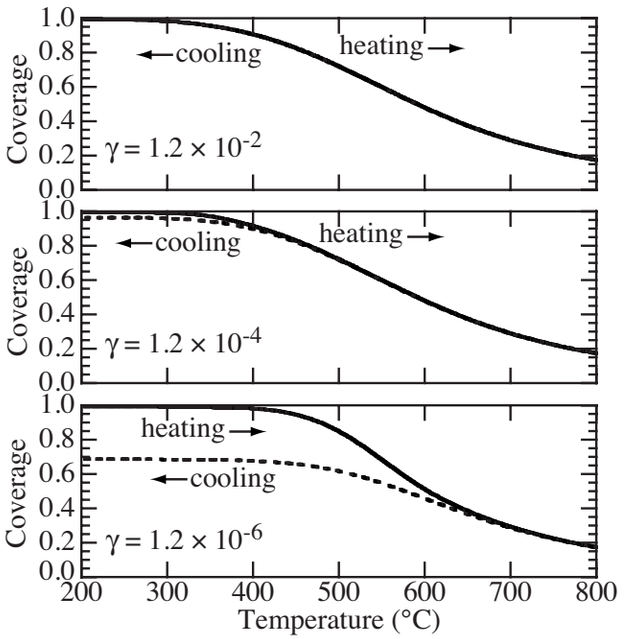

Figure 7. Predicted OH^-(Zr) coverages on YSZ from chemisorbed gas-phase H_2O computed for heating at 5°C/h from 20 to 800°C, followed by cooling at 5°C/h back to 20°C. The ambient gas mixture is 3% H_2O in oxygen at atmospheric pressure.

The rate of Reaction 35 is set to reproduce the ion (or vacancy) hopping rate implied by the known conductivity or vacancy diffusion in a YSZ crystal. The vacancy diffusion coefficient can be written as[35]

$$D_{V_O} = \zeta a_0^2 \nu_0 \exp\left(-\frac{E}{RT}\right) \quad [42]$$

where ζ is a geometric correction factor, a_0 is the distance between equivalent sites, E is an activation energy, and ν_0 is the attempt frequency. The hopping frequency ν is related to the attempt frequency ν_0 as

$$\nu = \nu_0 \exp\left(-\frac{E}{RT}\right) \quad [43]$$

Using the vacancy diffusion coefficient reported by Sasaki and Maier (9.5 mol % Y_2O_3-stabilized ZrO_2) as[36]

$$D_{V_O} = 1.9 \times 10^{-2} \exp\left(-\frac{0.83\ \text{eV}}{k_B T}\right)\ \text{cm}^2/\text{s} \quad [44]$$

assuming that $\zeta = 1$ and $a_0 = 5.14$ Å, the attempt frequency is $\nu_0 = 7.3 \times 10^{12}$ Hz. The A factor for Reaction 35 is taken as the attempt frequency and the activation energy is assumed to be the same as for the vacancy diffusion, $E = 80.1$ kJ/mol (0.83 eV). This rate effectively maintains the vacancy-exchange reaction close to equilibrium.

In evaluating the rate of progress for Reaction 35, the oxygen ion and vacancy activities in the bulk YSZ are taken as their mole fractions, $X_{O_O^{2-}} = 0.9626$ and $X_{V_O} = 0.0374$. The activities of surface species (χ) and $O^{2-}(\chi)$ are evaluated as the molar concentrations (i.e., the product of the fractional surface coverage θ_k and the available site density Γ).

The role of Reaction 38 is to rapidly shift $OH^-(\chi)$ to OH^-(Zr). Because Reaction 38 is intended to remain nearly equilibrated, it was simply assigned a high rate.

Adsorption reactions are relatively slow. Chemisorption of H_2O is sluggish, requiring long equilibration times. Less is known about the kinetics of hydrogen chemisorption, but it is likely to be similarly slow. The rate for water adsorption (i.e., Reaction 37) is expressed as a sticking probability

$$\gamma = \gamma_0 e^{-E/RT} \quad [45]$$

The activation energy for the H_2O chemisorption reaction is taken to be 86.8 kJ/mol.[32] In the study by Raz et al., thermogravimetric measurements were carried out for heating and cooling rates of ±5°C/h. At this rate the OH coverage shows a small hysteresis behavior.

As a means to estimate the value of γ_0, the thermogravimetric experiments of Raz et al.[32] were simulated for several different γ_0 values, as shown in Fig. 7. The time-dependent coverage of OH^-(Zr) by the chemisorption of gas-phase H_2O was computed by integrating the transient mass-action kinetics (Table IV) with an imposed time-temperature profile consisting of heating at 5°C/h to 800°C, followed by cooling at the same rate. The ambient gas composition is 3% H_2O in oxygen at atmospheric pressure. For $\gamma_0 = 1.2 \times 10^{-2}$, the adsorption/desorption kinetics are sufficiently fast that there is little hysteresis at this heating/cooling rate. At the other extreme, if $\gamma_0 = 1.2 \times 10^{-6}$, then the kinetics are sluggish, and substantial hysteresis is observed. Neither is consistent with the observations of Raz et al. However, taking $\gamma_0 = 1.2 \times 10^{-4}$ results in a

Table IV. Heterogenous reaction mechanism on a YSZ surface. $\Delta H°$ and $\Delta G°$ are evaluated at 700°C. Available site density for the (Zr) sites and (χ) sites is $\Gamma = 1.25 \times 10^{-9}$ mol/cm^2. The forward rate coefficients are given in Arrhenius form as $k = Ae^{-E/RT}$.

Reaction	A or γ_0 (mol,cm,s)	E (kJ/mol)	$\Delta H°$ (kJ/mol)	$\Delta G°$ (kJ/mol)
35	7.3×10^{12}	80.1	0.0	8.6
37	1.2×10^{-4}[a]	86.8	−80.0	38.9
38	2.0×10^{10}	0.0	35.0	−35.0
41	1.0×10^{-8}[a]	20.0	−17.8	121.7

[a] Sticking probability in the form of $\gamma = \gamma_0 e^{-E/RT}$.

small hysteresis and is consistent with the experimental observations. Thus, the value $\gamma_0 = 1.2 \times 10^{-4}$ is adopted here.

A net result of the charge-transfer process is the production of gas-phase $H_2O(g)$. It is interesting to explore the potential role of H_2O desorption from the YSZ surface via hydroxyl recombination (i.e., reverse of Reaction 37). Hydroxyl coverage on the YSZ surface could be the result of at least two processes: One being the result of thermal chemistry with the gas phase and the other being the result of charge-transfer chemistry at the TPB. Gas-phase interactions affect the YSZ surface uniformly, but charge-transfer chemistry is concentrated at the TPB.

Mizusaki et al. reported anodic currents up to 0.1 mA/cm^2 with a $H_2O(g)$ partial pressure of 850 Pa. Using their reported value of λ_{TPB} (303 cm/cm^2), this is equivalent to a current per unit TPB length of 3×10^{-4} mA/cm. The production rate of water per unit TPB length is then 2×10^{-12} mol/cm s.

At equilibrium with $H_2O(g)$ at 850 Pa and 800°C, the hydroxyl coverage is approximately 10% [i.e., $OH^-(\chi) = 2.22 \times 10^{-4}$ and $OH^-(Zr) = 0.10$]. Under equilibrium conditions the water desorption rate from the YSZ surface equals the chemisorb rate. Assuming that $\gamma_0 = 1.2 \times 10^{-4}$, the equilibrium adsorption/desorption rate of $H_2O(g)$ is 3.87×10^{-12} mol/cm^2 s.

Now, for example, suppose that as a result of charge-transfer reactions at the TPB, the OH^- coverage on the YSZ is increased uniformly by a factor of 8 [i.e., $OH^-(\chi) = 1.78 \times 10^{-3}$ and $OH^-(Zr) = 0.80$] out to some distance L from the TPB. Over this distance the water desorption rate (reverse of Reaction 37) would be approximately 3.2×10^{-10} mol/cm^2 (increased by a factor of 64). To produce the net $H_2O(g)$ desorption rates required to support the observed current densities, the distance L would have to be approximately 3 mm. This greatly exceeds the spacing between lines in the pattern-anode experiments. In any case it is difficult to envision a surface-diffusion mechanism by which the surface could be uniformly hydroxylated out to such a large distance from the TPB. Even if the estimate of γ_0 were low by an order of magnitude, the distance L would still be 300 μm, which again is far too large.

Because of slow chemisorption–desorption kinetics, one must conclude that $H_2O(g)$ produced during electrochemical oxidation cannot be due to hydroxyl recombinative desorption from the YSZ surface. However, it is possible that water is formed on the YSZ surface and desorbs directly to the gas phase. Indeed, this is the mechanism proposed initially by de Boer[3] and used in the mechanisms developed by Goodwin and colleagues[15,16,19] and Bessler and colleagues.[18,20] It is also possible that the charge-transfer chemistry at the TPB produces H_2O on the Ni surface (or rapidly transfers to the Ni from the TPB). In this case, which is assumed here (Table V), the desorption kinetics from the Ni surface are known (Table I).

Surface diffusion on YSZ.— The measured oxygen diffusion coefficient on ZrO_2 can be represented as

$$D_O = 5.846 \times 10^{-11} \exp(-E_O/RT) \ (\text{cm}^2/\text{s}) \qquad [46]$$

where $E_O = 49$ kJ/mol.[37,38] At 700°C, $D_O = 1.37 \times 10^{-13}$ cm^2/s. The surface diffusion coefficient of hydrogen on the ZrO_2 surface is very uncertain with reported values ranging from 10^{-10} to 10^{-4} cm^2/s.[39,40] The present model uses surface-diffusion coefficients for H and OH as 5×10^{-8} cm^2/s. However, the results depend very weakly upon this value.

Solution Algorithm

The governing equations represent surface diffusion, heterogeneous surface reactions, and electrochemical charge transfer at the interface between the Ni and YSZ surfaces. Each of the surfaces has several adsorbed species, which may react among themselves and with the adjacent gas phase. The gas-phase composition is held fixed for the results shown in this paper. At the TPB, formed at the interface between the Ni and YSZ surfaces, both charge-transfer and thermal reactions can proceed. The species fluxes produced and consumed by these reactions form boundary conditions for the reaction-diffusion equations. The charge-transfer reaction rates depend upon the electric-potential difference between the Ni and YSZ across the TPB.

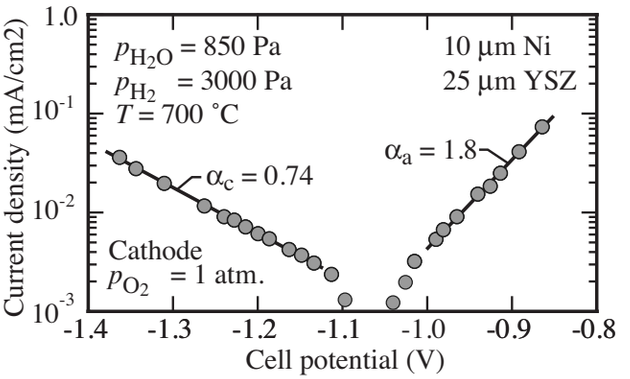

Figure 8. DC polarization data from Mizusaki et al.[1] (symbols) for p_{H_2} = 3000 Pa, p_{H_2O} = 850 Pa, and T = 700°C. The solid lines show the linear fits used to determine α_a and α_c.

Faradaic current is produced (or consumed) by the charge-transfer reactions. Current can be supplied to (or removed from) the system via an external source. The external current and faradaic current both appear in Eq. 4, which governs the charge on the Ni electrode. Knowing the charge q_{dl}, the electrode electric potential ϕ_a can be determined using the double-layer capacitance C_{dl}. Under steady-state conditions $\phi_a - \phi_{e,a} = q_{dl}/C_{dl}$.

The computational model is implemented in both transient and steady forms. In both cases, all the spatial derivatives are discretized using a finite-volume formulation on a one-dimensional mesh network that spans the Ni and YSZ surfaces. The transient problem is solved via a method-of-lines approach using either Cvode[41] or Limex[42] as the ordinary-differential-equation solution software. The steady-state solution can be achieved by solving the transient problem to a steady state, which is a computationally robust approach. Alternatively, the steady-state problem can be solved directly using a modified Newton iteration. The software used here is the Cantera implementation of a hybrid Newton method.[21,43]

The chemistry and transport are handled by the Cantera software,[44] which is written in C++ and is highly object oriented. This software provides the capability to define bulk materials, surfaces, and interfaces, each of which may involve different reaction chemistry among different species.

Interpretation of Mizusaki Experiments

Mizusaki et al.[1] reported pattern-anode measurements that provide a great deal of information that can be used to understand the fundamental mechanism of hydrogen electrochemical oxidation. The dc polarization measurements were made with fixed gas compositions and anode potentials E_a. Reaction orders can be identified by varying the partial pressures of H_2 or H_2O, while holding the other partial pressures and the anode potential E_a constant. The partial pressures were varied independently by using mixtures of H_2 and H_2O that are dilute in argon. Typical gas compositions were, for example, 3000 Pa of H_2, 1700 Pa of H_2O, and 95,300 Pa of argon. Equally important, the anode potential was fixed relative to a cathode-side reference electrode. The Ni patterns in the Mizusaki experiments were 10 μm wide and separated by 25 μm of YSZ. The experiments were operated under isothermal conditions at 700°C. Mizusaki et al. reported a TPB length per unit area of 303 cm/cm^2.

DC polarization.— Figure 8 reproduces a representative dc polarization curve as reported by Mizusaki et al. The measurements

clearly show the exponential character of the overpotentials with sufficient anodic or cathodic polarization. The anodic and cathodic branches can be fit in Tafel form

$$i_a = \exp\left(\frac{\alpha_a F E_a}{RT}\right), \quad i_c = \exp\left(-\frac{\alpha_c F E_a}{RT}\right) \qquad [47]$$

which yields $\alpha_a = 1.8$ and $\alpha_c = 0.74$.

At least one major conclusion can be drawn from Fig. 8 even before modeling the experiments. The results show that $\alpha_a + \alpha_c \approx 2.5$, which is significantly greater than the maximum value of 2 that would result from any reaction mechanism in which two elementary charge-transfer reactions proceed in series to produce the net transfer of two electrons for the global half-cell hydrogen-oxidation reaction. Therefore, these data suggest that at least two charge-transfer pathways are proceeding in parallel.

Reaction mechanisms.— Consider the situation when the cell is operating well away from the near-equilibrium conditions that prevail near open circuit (i.e., where anodic and cathodic currents nearly balance). At large anodic or cathodic polarizations, the rate-limiting step essentially proceeds irreversibly in either the anodic or cathodic direction, depending upon the sign of the polarization. It follows that the current should depend upon gas-phase partial pressures and electrode potential in ways consistent with the rate-limiting step. For example, reaction order should depend upon the stoichiometry of the rate-limiting reaction.

There can be at least two possible explanations for the observed exponential response at large polarization. Either the rate of the rate-limiting process is exponential in E_a, or the activity of some reactant species is, or both are. The first possibility would occur if charge transfer is rate limiting, and the second could occur in the opposite limit of a fast, equilibrium, charge-transfer process. Models are used to consider the consequences of both possibilities.

Fast oxygen transfer.— Mizusaki et al.[1] proposed that their experimental results could be explained by assuming that a global charge-transfer reaction

$$O_O^{2-} + (Ni) \rightleftharpoons O(Ni) + V_O + 2e^- \qquad [48]$$

is fast and remains close to equilibrium. In this scenario, mobile oxygen ions from the YSZ readily cross the TPB to adsorb on the nickel surface, releasing two excess electrons into the conduction band of the nickel anode. This process also proceeds readily in reverse with surface-adsorbed oxygen on the nickel surface crossing the TPB along with two electrons to fill a vacancy in the oxide lattice.

The equilibrium condition for Reaction 48 may be stated in terms of electrochemical potentials as

$$\mu_{O(Ni)} - \mu_{(Ni)} - 2F(\phi_a - \phi_{e,a}) = \mu_{O_\chi^{2-}} - \mu_{V_O} \qquad [49]$$

For the low current densities encountered in patterned-anode experiments, ϕ_e is assumed spatially uniform within the bulk electrolyte outside the double layers. This is particularly valid if a single-crystal electrolyte is used, as in the study by Mizusaki et al.

On the cathode side of the electrolyte disk, a reference electrode provides a constant reference potential because it draws negligible current and is exposed to a fixed oxygen ambient. Therefore, at the reference electrode, the global oxygen-reduction reaction (i.e., Reaction 1) is assumed to be equilibrated. In this case, the equilibrium condition provides that

$$\tfrac{1}{2}\mu_{O_2(g)} - 2F(\phi_c - \phi_{e,c}) = \mu_{O_O^{2-}} - \mu_{V_O} \qquad [50]$$

Here ϕ_c is the electrical potential of the cathode.

Equating the left-hand sides of Eq. 49 and 50 yields a global equilibrium condition as

$$\mu_{O(Ni)} - \mu_{(Ni)} - 2F(\phi_a - \phi_c) = \tfrac{1}{2}\mu_{O_2(g)} \qquad [51]$$

Substituting the appropriate forms for the chemical potentials, namely

$$\mu_{O(Ni)} = \mu^\circ_{O(Ni)} + RT \ln \theta_{O(Ni)} \qquad [52]$$

$$\mu_{(Ni)} = \mu^\circ_{(Ni)} + RT \ln \theta_{(Ni)} \qquad [53]$$

$$\mu_{O_2(g)} = \mu^\circ_{O_2(g)} + RT \ln p_{O_2(g)} \qquad [54]$$

an equilibrium expression can be written for the coverage of oxygen on nickel at the TPB

$$\theta_{O(Ni)} = \theta_{(Ni)} p_{O_{2,c}}^{1/2} \exp\left(-\frac{\Delta G^\circ}{RT}\right)\exp\left(-\frac{2FE_{cell}}{RT}\right) \qquad [55]$$

Here

$$\Delta G^\circ = \mu^\circ_{O(Ni)} - \mu^\circ_{(Ni)} - \tfrac{1}{2}\mu^\circ_{O_2(g)} \qquad [56]$$

is the standard free energy of adsorption of oxygen on nickel and $E_{cell} = \phi_c - \phi_a$.

If one postulates, as Mizusaki et al. did, that under anodic polarization the rate-limiting step is the direct reaction of $H_2(g)$ with O(Ni) via

$$H_2(g) + O(Ni) \rightarrow H_2O(g) + (Ni) \qquad [57]$$

then the anodic current density should have the form

$$i = 2Fk(T)p_{H_2} \exp\left(-\frac{2FE_{cell}}{RT}\right) \qquad [58]$$

where $k(T)$ incorporates the free energy of adsorption, the open-site fraction, and kinetic parameters for Reaction 57. This expression for the current density does represent many aspects of the experimental observations; that is, a symmetry factor of near 2, and reaction orders with respect to H_2 and H_2O of 1 and zero, respectively.

Despite the agreement with observation in some respects, this proposed mechanism also has potential shortcomings that Mizusaki et al. did not explore. Because they considered only the forward direction of the rate-limiting reaction, the proposed mechanism cannot be used to explain their measurements under cathodic polarization. For this case, they postulated an entirely different rate-limiting process. Unfortunately, equating the anodic and cathodic currents does not yield the correct dependence on gas composition for equilibrium behavior under open-circuit conditions. Therefore, the proposed anodic and cathodic rate expressions cannot be universally valid; in particular, they cannot be valid at low polarization, where both anodic and cathodic currents are significant.

The proposal of Mizusaki et al. (i.e., Eq. 57) has other shortcomings. It considers none of the reactions on the nickel surface that are responsible for nickel's high activity in heterogeneous catalysis (discussed in the previous section). Moreover, the spatial extent of the surface-oxygen coverage on the nickel surface must depend strongly upon the diffusion coefficient for O(Ni) on nickel. As discussed previously, the area adjacent to the TPB over which the O(Ni) coverage is elevated depends upon current density. This behavior should introduce another factor into Eq. 58 that should serve to perturb the symmetry factor from a value of 2.

Alternative Charge-Transfer Mechanisms

Table V lists three potential reaction mechanisms that may be able to explain charge-transfer pathways at the Ni-YSZ TPB. Given a postulated set of reactions, the model developed in this paper can be exercised to predict polarization characteristics and produce Tafel plots. The predicted Tafel plots can be compared directly to the Mizusaki measurements.

Reaction-rate parameters that provide the best fit to the Mizusaki measurements are identified for each of the potential mechanisms. For each of the potential mechanisms, the adjusted parameters are Arrhenius A factors and the anodic symmetry factors β_a for each reaction. Because all the Mizusaki measurements were taken at 700°C, there are insufficient data to establish the temperature dependencies. Thus, activation energies for the charge-transfer reactions are not considered. The approach assumes that the chemistry

Table V. Alternative charge-transfer pathways. The rate constants *A* are evaluated at 700°C.

Reaction	*A* (mol,cm,s)	β_a
Oxygen spillover		
$O^{2-}(\chi) \rightleftharpoons O^{-}(\chi) + e^{-}$ [59]	2.66×10^{06}	0.500
$O^{-}(\chi) + (Ni) \rightleftharpoons O(Ni) + (\chi) + e^{-}$ [60]	2.66×10^{08}	0.500
Hydrogen spillover (symmetry factors fixed at $\beta = 1/2$)		
$H(Ni) + O^{2-}(\chi) \rightleftharpoons OH^{-}(\chi) + (Ni) + e^{-}$ [61]	5.00×10^{12}	0.500
$H(Ni) + OH^{-}(\chi) \rightleftharpoons H_2O(Ni) + (\chi) + e^{-}$ [62]	4.09×10^{09}	0.500
Hydrogen spillover (single channel)		
$H(Ni) + O^{2-}(\chi) \rightleftharpoons OH^{-}(\chi) + (Ni) + e^{-}$ [61]	5.00×10^{12}	0.500
$H(Ni) + OH^{-}(\chi) \rightleftharpoons H_2O(Ni) + (\chi) + e^{-}$ [62]	1.55×10^{09}	0.300
Hydrogen spillover (dual channel)		
$H(Ni) + O^{2-}(\chi) \rightleftharpoons OH^{-}(\chi) + (Ni) + e^{-}$ [63]	5.00×10^{12}	0.500
$H(Ni) + OH^{-}(\chi) \rightleftharpoons H_2O(Ni) + (\chi) + e^{-}$ [64]	8.50×10^{08}	0.250
$H(Ni) + OH^{-}(\chi) \rightleftharpoons H_2O(Ni) + (\chi) + e^{-}$ [65]	1.36×10^{10}	0.800

and transport on the Ni and YSZ surfaces are established, as discussed earlier in the paper and is therefore not part of the parameter identification.

Oxygen spillover.— As an alternative to the mechanism proposed by Mizusaki et al., assume that charge transfer is rate limiting. If this is the case, the values of α_a and α_c (see Fig. 8) strongly suggest that the charge transfer occurs via two (or more) parallel charge-transfer pathways, each of which is itself a two-step sequential process. The reasoning to support this suggestion is as follows. For a single elementary charge-transfer reaction (i.e., transferring only one electron), the value of the symmetry factor β is usually assumed to be approximately 1/2. If all charge transfer is accomplished by a single elementary reaction, the result would be $\alpha_a = \beta$ and $\alpha_c = 1 - \beta$. Figure 8 clearly shows that this is not observed.

Suppose, however, that a fast charge-transfer reaction that is nearly in equilibrium produces an intermediate species at the TPB, which then reacts via a second, relatively slow, charge-transfer reaction to complete the transfer of two electrons. Such a process might occur, for example, via Reactions 59 and 60

$$O^{2-}(\chi) \rightleftharpoons O^{-}(\chi) + e^{-} \quad [59]$$

$$O^{-}(\chi) + (Ni) \rightleftharpoons O(Ni) + (\chi) + e^{-} \quad [60]$$

with the rate of the first reaction being fast, and the rate of the second reaction being slow. Such a mechanism has been proposed in prior literature.[9,45]

The oxygen-spillover charge-transfer mechanism is based upon oxygen transferring across the TPB from the YSZ surface to the Ni. The first step transfers one electron from an $O^{2-}(\chi)$ on the YSZ surface into the Ni, leaving a singly ionized oxygen on the YSZ. The second rate-limiting step transfers the oxygen ion across the TPB onto the Ni surface, delivering another electron into the Ni and opening a vacancy on the YSZ. This scenario is plausible because the first (fast) reaction involves only an electron transfer, while the second (slow) reaction requires moving an oxygen ion across the TPB interface.

Assuming that Reaction 59 is sufficiently fast that it can be approximated to be in equilibrium and that the $O^{-}(\chi)$ coverage is small (i.e., $\theta_{O^{-}(\chi)} \ll 1$), it follows that

$$\theta_{O^{-}(\chi)} \propto \exp\left(\frac{FE_a}{RT}\right) \quad [66]$$

If the second reaction is rate limiting, it will proceed irreversibly in the forward direction (i.e., forward rate much greater than reverse rate) at a rate proportional to

$$i \propto \theta_{O^{-}(\chi)} \exp\left(\frac{\beta_{60} FE_a}{RT}\right) \quad [67]$$

Substituting Eq. 66 into Eq. 67 reveals that $\alpha_a = 1 + \beta_{60}$.

On the cathodic branch, the reactions run in reverse with the slow Reaction 60 occasionally transferring an oxygen from the Ni to the YSZ, which is then immediately converted into $O^{2-}(\chi)$ by Reaction 59. In this case, $\alpha_c = 1 - \beta_{60}$.

If instead Reaction 60 is fast and Reaction 59 is rate limiting, then a similar analysis shows that the result is $\alpha_a = \beta_{59}$ and $\alpha_c = 2 - \beta_{59}$. Therefore, a two-step charge-transfer process can result in an asymmetric polarization curve, unlike a single-step process that would have $\alpha_a = \beta$ and $\alpha_c = 1 - \beta$.

Figure 9 shows a comparison of the oxygen-spillover mechanism (i.e., Reactions 59 and 60). In this comparison, both reactions are constrained to have symmetry factors $\beta_a = 1/2$. At fixed H_2 partial pressure the anodic branch is represented reasonably well. However, elsewhere this mechanism represents the data poorly. The result is particularly poor on the cathodic branches, especially the reaction orders. On the cathodic branches, the model shows much stronger dependence upon the H_2O and H_2 partial pressures than the data do. On the anodic branches, the model-predicted H_2O reaction order is consistent with the data (lower panel, Fig. 9). However, the model predicts nearly zero dependence for the H_2 partial pressure on the anodic branch, whereas the data show significant dependence on the H_2 partial pressure (upper panel, Fig. 9). From these results, oxygen moving from the YSZ to the Ni is not a likely mechanism to explain the charge-transfer process.

Hydrogen spillover, single channel.— The hydrogen-spillover pathway, first suggested by de Boer,[3,15] is a two-step mechanism that first transfers a proton from the Ni to an oxygen ion $O^{2-}(\chi)$ on the YSZ surface, producing a hydroxyl ion $OH^{-}(\chi)$ on the YSZ and delivering one electron to the Ni. This reaction is followed by the rate-limiting reaction that transfers another proton from the Ni surface to the hydroxyl $OH^{-}(\chi)$ on the YSZ. The rate (i.e., the *A* factor) of the first reaction (Reaction 61 in Table V) is not too important as long as its net rate remains fast compared to the rate-limiting second reaction (Reaction 62). The products of the second reaction are written as H_2O on the Ni and another electron delivered into the Ni. Because the product $H_2O(Ni)$ is on the Ni surface, the second step could be effectively viewed as a transfer of the hydroxyl ion to the Ni surface. H_2O readily desorbs from the Ni surface according to the reverse of Reaction 22 (Table I).

The mechanism proposed by de Boer produces adsorbed water on the YSZ surface, and the water desorbs directly from that surface.[3] In the mechanism proposed here the YSZ surface is composed of two site types (χ) and (Zr). Based upon the results of Raz et al.,[32] chemisorbed H_2O takes the form of $OH^{-}(\chi)$ and $OH^{-}(Zr)$. In other words, the present mechanism does not include a species such as $H_2O(YSZ)$. Because the water readily desorbs, the results are insensitive to the details of the water desorption.

Figure 10 illustrates the performance of the hydrogen-spillover mechanism with the symmetry factors for both reactions fixed at $\beta = 1/2$. The reaction *A* factors are adjusted to achieve a best fit to the measurements. The mechanism represents the anodic branches well. On the cathodic branches, however, the model significantly underpredicts the charge-transfer rates, especially with strong cathodic bias. Moreover, the cathodic symmetry factors are significantly smaller than the data. However, the cathodic reaction orders are reasonably consistent with the data. That is, the charge-transfer rate depends weakly upon the H_2 partial pressure (upper panel, Fig.

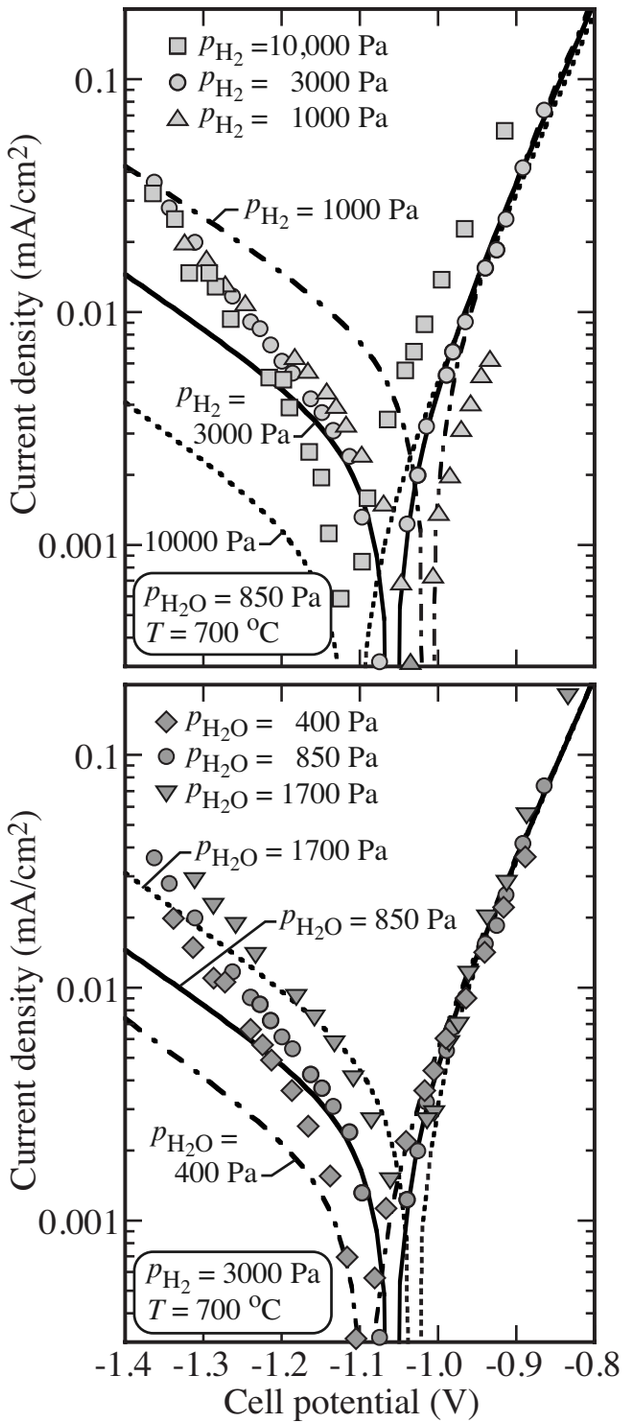

Figure 9. Comparison between the oxygen-spillover charge-transfer model and the Mizusaki measurements. The upper panel is for fixed H_2O partial pressure and varying H_2 partial pressure. The lower panel is for fixed H_2 partial pressure and varying H_2O partial pressure. The system is isothermal at 700°C and 1 atm.

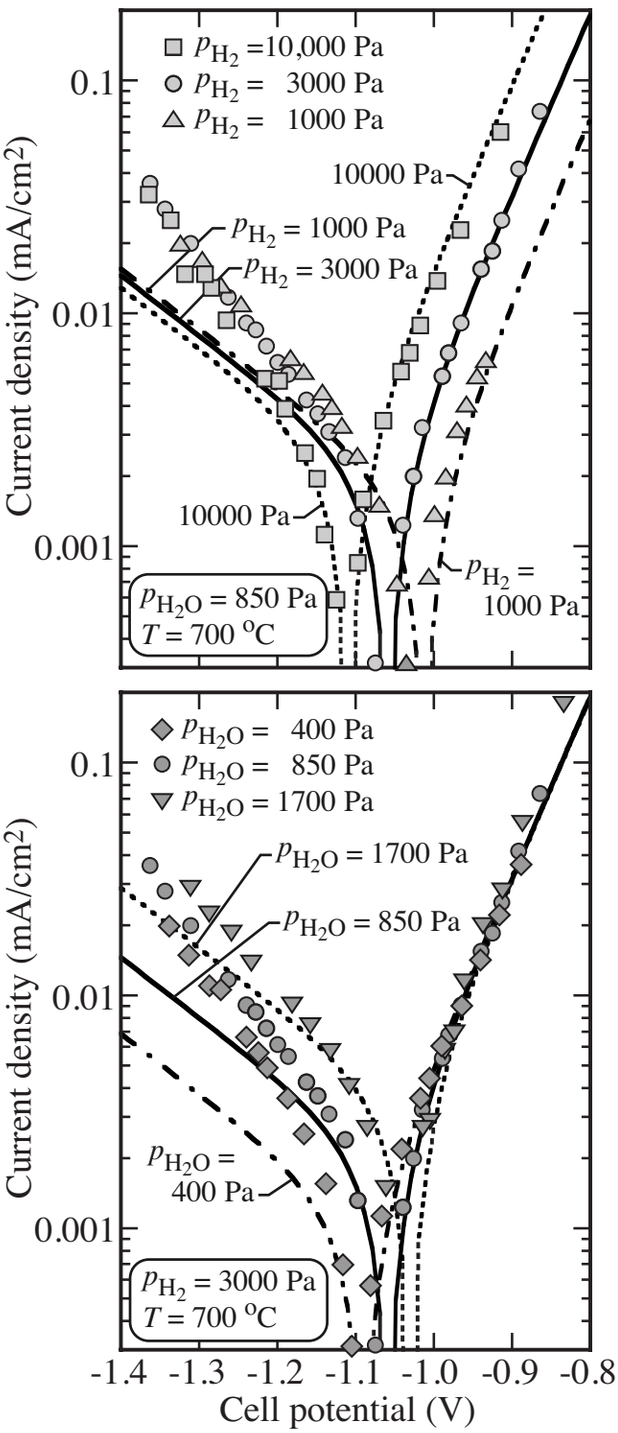

Figure 10. Comparison between the single-channel hydrogen-spillover charge-transfer model and the Mizusaki measurements. The symmetry factors for both reactions are fixed at $\beta = 1/2$, and the reaction A factors are adjusted to achieve a best fit to the data. The upper panel is for fixed H_2O partial pressure and varying H_2 partial pressure. The lower panel is for fixed H_2 partial pressure and varying H_2O partial pressure. The system is isothermal at 700°C and 1 atm.

10) and moderately on the H_2O partial pressure (lower panel, Fig. 10). Despite the lack of agreement at large cathodic bias, the hydrogen-spillover mechanism provides a substantially better representation of the data than the oxygen-spillover mechanism does.

Seeking to improve the performance of the hydrogen-spillover mechanism, the symmetry factor for the rate-limiting reaction (i.e., Reaction 62) is varied away from $\beta = 1/2$. Figure 11 shows the performance with $\beta_{a,62} = 0.3$. Lowering the anodic symmetry factor significantly improves the performance of the mechanism on the cathodic branches, yet has a nearly negligible effect on the anodic

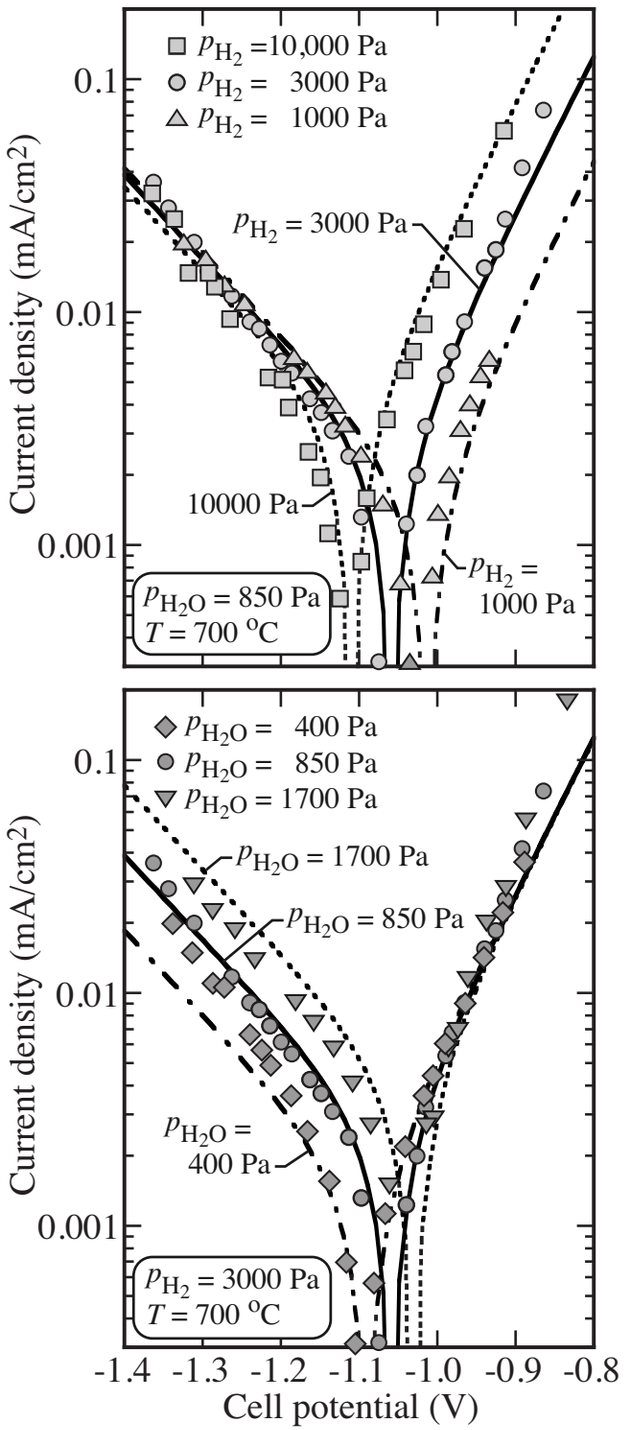

Figure 11. Comparison between the single-channel hydrogen-spillover charge-transfer model and the Mizusaki measurements. The *A* factors for both reactions and the anodic symmetry factor for the rate-limiting reaction (i.e., 62) are adjusted to achieve a best fit to the data. The upper panel is for fixed H_2O partial pressure and varying H_2 partial pressure. The lower panel is for fixed H_2 partial pressure and varying H_2O partial pressure. The system is isothermal at 700°C and 1 atm.

branches. Although the fundamental basis for a reduced anodic symmetry factor is unclear, the predictive performance of the mechanism is substantially improved compared to using a symmetry factor of $\beta_a = 1/2$.

Modified Butler–Volmer formulation.— Assuming that Reaction 62 is the rate-limiting step, Zhu et al.[15] derived a modified Butler–Volmer formulation for the two-step single-channel hydrogen-spillover charge-transfer pathway as

$$i_{e,BV} = i_0\left[\exp\left(\frac{\alpha_a F\eta_{act}}{RT}\right) - \exp\left(-\frac{\alpha_c F\eta_{act}}{RT}\right)\right] \qquad [68]$$

where $\alpha_a = 1 + \beta_{a,62}$ and $\alpha_c = \beta_{c,62}$ are the anodic and cathodic symmetry factors, and η_{act} is the activation overpotential. The exchange current density i_0 in the Butler–Volmer equation represents the temperature and species dependencies for the charge-transfer reactions. Based upon a set of underpinning elementary reaction for the Ni and YSZ surfaces and assumptions about rate-limiting steps, Zhu et al.[15] derived a functional form for the exchange current density for hydrogen oxidation i_{0,H_2} as

$$i_{0,H_2} = i^*_{H_2}\frac{(p_{H_2}/p^*_{H_2})^{(1-\alpha_a/2)}(p_{H_2O})^{\alpha_a/2}}{1 + (p_{H_2}/p^*_{H_2})^{1/2}} \qquad [69]$$

The parameter $p^*_{H_2}$ depends upon hydrogen adsorption/desorption rates and the parameter $i^*_{H_2}$ is assigned empirically to fit measured polarization data.

Figure 12 compares the Butler–Volmer formulation with the Mizusaki polarization data. The symmetry factors in the modified Butler–Volmer equation are $\alpha_\alpha = 1.3$ and $\alpha_c = 0.7$. The value of $i^*_{H_2} = 0.124$ A/cm^2 achieves a best fit to the Mizusaki data. Figure 12 shows that the modified Butler–Volmer formulation generally represents the experimental data quite well.

The model results shown in Fig. 12 are simply graphs of the modified Butler–Volmer equation in Tafel form. In other words, there is no consideration for surface diffusion, as there is in all the other modeling results. The relatively good representation of Mizusaki data suggests that surface diffusion is not playing an important role in the charge-transfer process. Indeed, as subsequently discussed, interpretation of the reaction-diffusion model also indicates that surface diffusion plays a weak role in the overall charge-transfer process.

The predicted H_2 reaction-order dependence on the cathodic branches is unanticipated (upper panel, Fig. 12). Although the reaction-order dependence is weak, the modified Butler–Volmer model predicts a trend that is different from both the data and the elementary reaction models. That is, on the cathodic branch, the model predicts that current density increases with increasing H_2 partial pressure. The data and all the elementary reaction mechanisms consistently show that the cathodic current density should decrease as the H_2 partial pressure increases. Nevertheless, the overall result shows that the modified Butler–Volmer model provides a reasonable representation of the data, especially for the anodic branches that are central to fuel-cell operation.

Hydrogen spillover, dual channel.— In an attempt to improve the hydrogen-spillover mechanism further, a dual-channel hydrogen spillover was considered. In this mechanism, the rate-limiting reaction appears twice but with different rate parameters (i.e., Reactions 64 and 65). The objective of this alternative is to enable different parallel rates for the same net reaction. The physical basis for such a possibility is that reactions with the same reactants and products may proceed by different pathways. For example, such behavior might occur with adsorbed species on different types of surface sites (e.g., steps or ledges). The *A* factors and symmetry factors for both reactions are taken as adjustable parameters.

Figure 13 illustrates the comparison between the model predictions using the dual-channel hydrogen-spillover mechanism and the Mizusaki data. Overall, this mechanism represents the measurements reasonably well. The current densities and Tafel slopes are accurately predicted for both anodic and cathodic polarizations. Particularly on the anodic branch, the dual-channel hydrogen-spillover

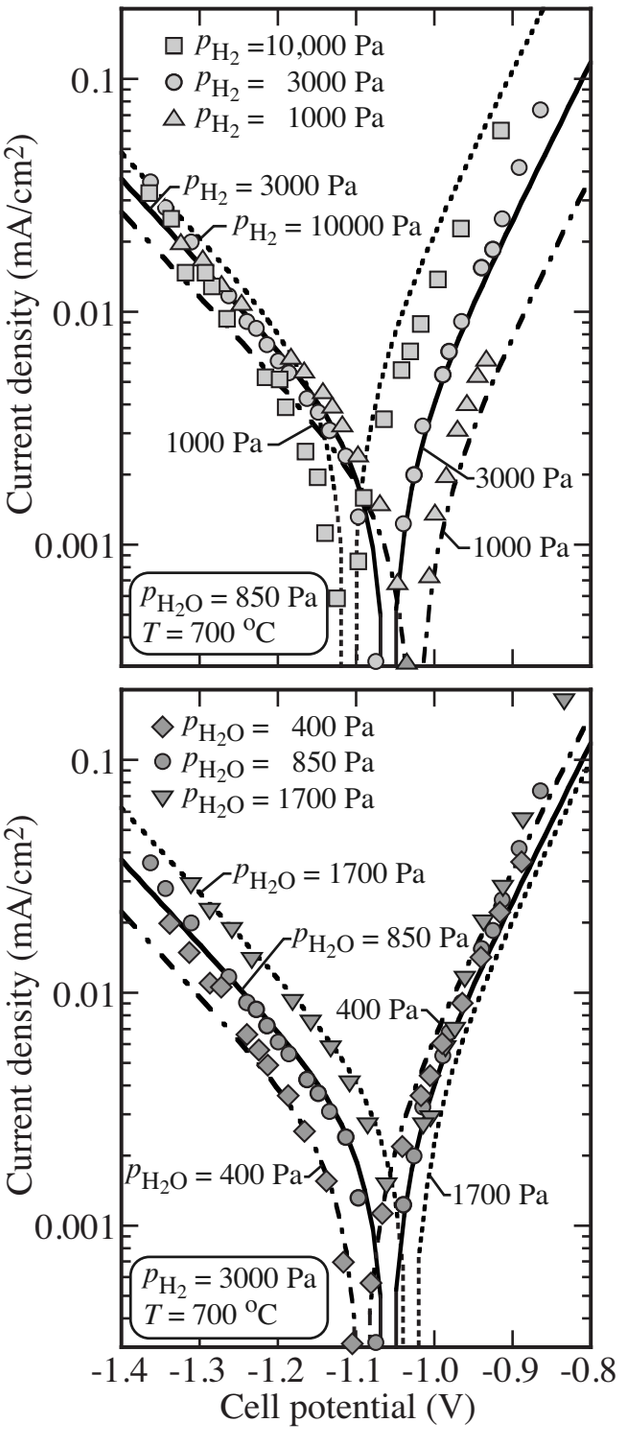

Figure 12. Comparison of the modified Butler–Volmer model based upon the single-channel hydrogen-spillover charge-transfer model and the Mizusaki measurements. The upper panel is for fixed H_2O partial pressure and varying H_2 partial pressure. The lower panel is for fixed H_2 partial pressure and varying H_2O partial pressure. The system is isothermal at 700°C and 1 atm.

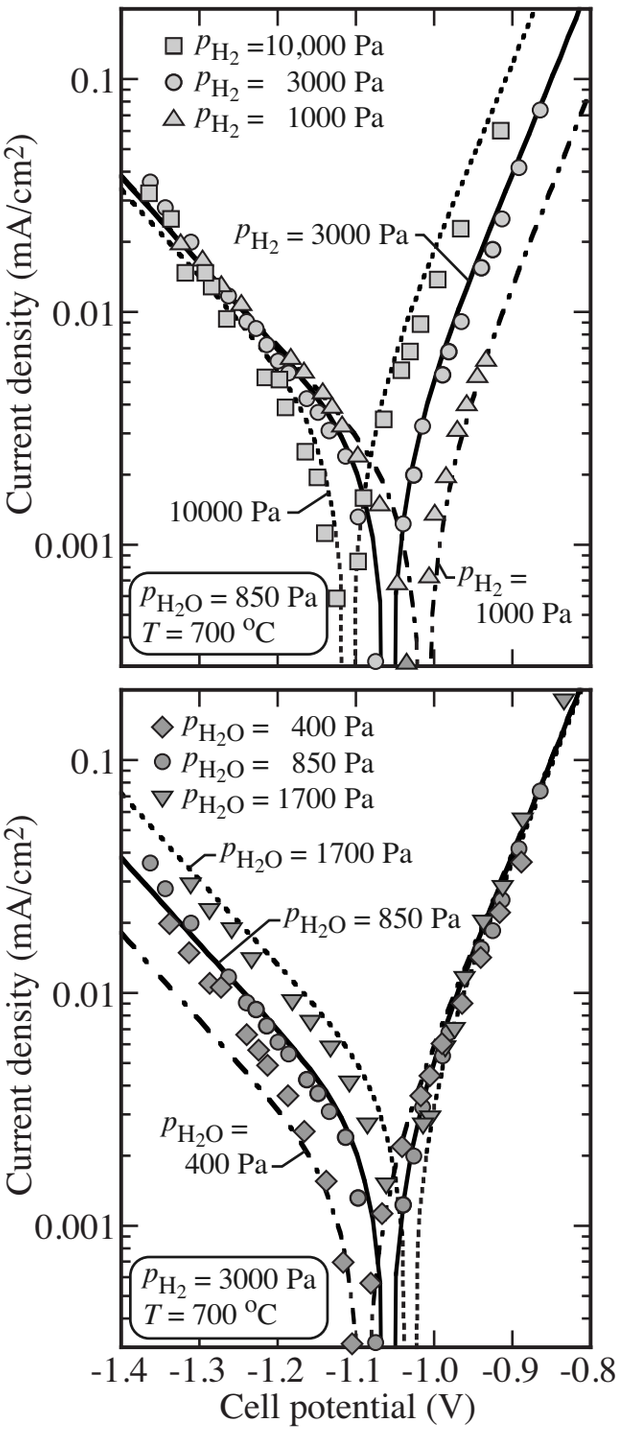

Figure 13. Comparison between the dual-channel hydrogen-spillover charge-transfer model and the Mizusaki measurements. The upper panel is for fixed H_2O partial pressure and varying H_2 partial pressure. The lower panel is for fixed H_2 partial pressure and varying H_2O partial pressure. The system is isothermal at 700°C and 1 atm.

mechanism shows improved performance at high anodic polarization. However, the predicted H_2O reaction order on the cathodic branch is somewhat stronger than is observed experimentally.

TPB behavior.— Figure 14 shows the surface-species coverages on both the Ni and YSZ surfaces at the TPB as functions of cell potential. Especially on the Ni surface, the coverages are nearly independent of the cell potential. This behavior indicates that the interaction of the Ni surface with the gas mixtures is much faster than that of the TPB charge-transfer rates.

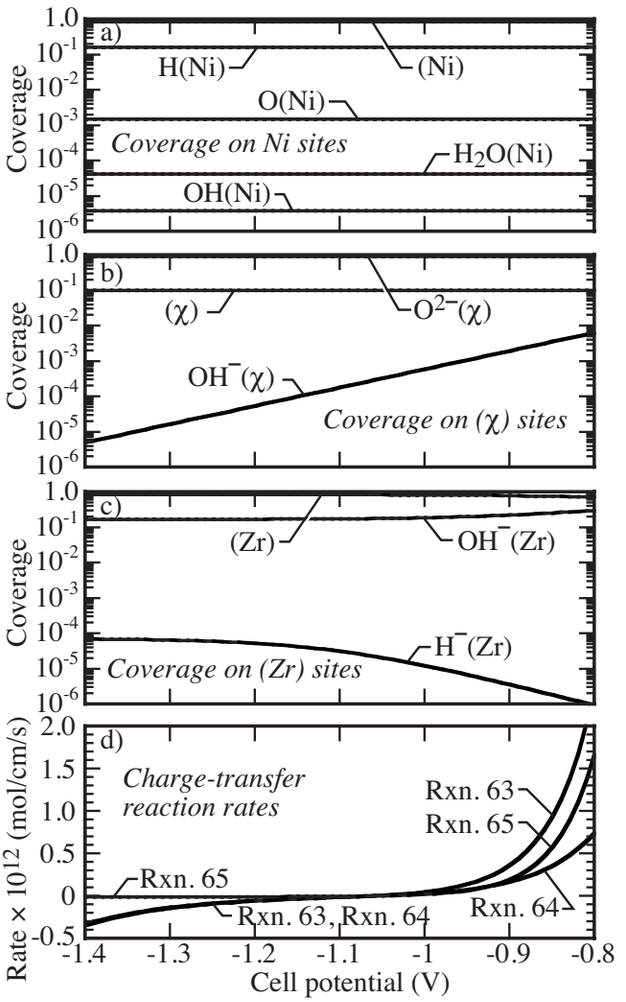

Figure 14. Surface species coverages on the Ni and YSZ surfaces at the TPB region by varying the cell potentials. The results are based upon the dual-channel hydrogen-spillover charge-transfer model. The rates of progress of the charge-transfer reaction steps at the TPB are illustrated in the bottom panel.

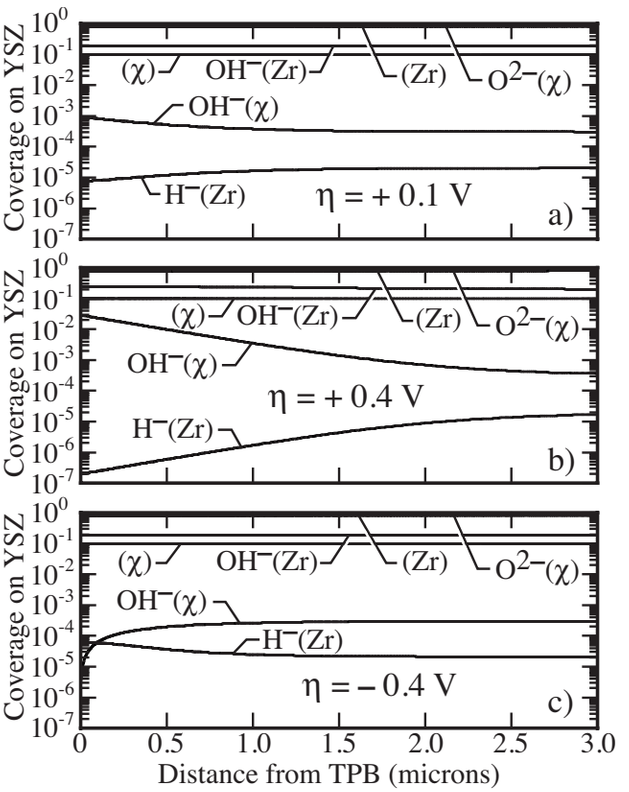

Figure 15. Predicted coverage profiles on the YSZ surface. The cell operates at the anode cell potentials of [(a), top] −0.96 [(b), middle] −0.66, and [(c), bottom] −1.46 V with a gas-phase composition of p_{H_2} = 3000 Pa and p_{H_2O} = 850 Pa. The corresponding anode activation overpotentials are η = 0.1, 0.4, and −0.4 V.

The YSZ surface has two types of sites (Fig. 4). The rate-limiting charge-transfer chemistry depends directly upon the coverage of $OH^-(\chi)$ (Reactions 64 and 65), which is present at low coverages. Figure 14b shows that the $OH^-(\chi)$ coverage depends directly upon the cell potential. Because of faster reaction rates between the surface oxygen and bulk oxygen, other species coverages on the oxygen sites are nearly independent of the cell potential. On the zirconium sites, the coverage of $OH^-(Zr)$ increases and $H^-(Zr)$ decreases from the cathodic polarization to the anodic polarization (Fig. 14c). Reaction 38 rapidly shifts $OH^-(\chi)$ to $OH^-(Zr)$, maintaining low coverage of $OH^-(\chi)$. Thus, as $OH^-(\chi)$ increases at anodic polarization, so too does the $OH^-(Zr)$ coverage. The low $H^-(Zr)$ coverage and Reaction 41 have a relatively small influence on the overall performance and could be neglected entirely.

Figure 14d also shows the rates of progress of the charge-transfer reaction steps. The rate of Reaction 63 is essentially the sum of Reactions 64 and 65 because Reaction 63 is fast and nearly equilibrated. On the cathodic branch, Reaction 64 is the rate-limiting step and the contribution from Reaction 65 is small. The difference between Reactions 64 and 65 lies in the symmetry factors, where the cathodic symmetry factor is $\beta_c = (1 - \beta_a) = 0.75$ for Reaction 64 and $\beta_c = (1 - \beta_a) = 0.2$ for Reaction 65. On the anodic branch, Reaction 65 becomes significantly more important. Compared to the cathodic branch, both Reactions 64 and 65 contribute to the charge-transfer rates. This is the reason that the dual-channel hydrogen-spillover mechanism can be adjusted to provide better performance at large anodic polarization but have little effect on the cathodic branch.

Reaction-Diffusion Processes Near TPB

The reaction-diffusion model shows that the charge-transfer process is confined to a small (nanometer scale) region near the TPB. Moreover, the results show that surface transport is not rate limiting even for the YSZ surface where surface-species diffusion coefficients are small compared to those on the Ni surface. On the Ni surface the coverage profiles are nearly uniform. The surface coverages are controlled primarily by reactions with the gas phase, which are relatively fast compared to surface diffusion rates.

Coverage gradients on the YSZ surface are larger than they are on the Ni surface but still relatively small. Importantly, the contribution of the surface diffusion to the charge-transfer rate at TPB is relatively small and not rate limiting. Consider, for example, the situation with a gas-phase composition of p_{H_2} = 3000 Pa and p_{H_2O} = 850 Pa and using the dual-channel hydrogen-spillover mechanism. Figure 15 shows the predicted coverage profiles on the YSZ surface with the anode overpotentials $\eta_a = 0.1$, 0.4, and −0.4 V. The corresponding current densities are 0.013, 3.74, and −0.063 mA/cm^2, and the electric potential differences are −0.96, −0.66, and −1.46 V, respectively.

With a relatively low anode overpotential of η = 0.1 V, the mole flux of $O^{2-}(\chi)$ consumed by charge transfer at TPB is 1.149 × 10^{-13} mol/cm s, which is much greater than the $O^{2-}(\chi)$ diffusion

mole flux of 1.237×10^{-15} mol/cm s. The $O^{2-}(\chi)$ consumed by the charge-transfer process is delivered primarily from the bulk O_O^{2-} via Reaction 35. Figure 15a shows that the most significant surface profile is that of $OH^-(\chi)$. Under anodic polarization, the $OH^-(\chi)$ is produced by Reaction 63, and then mostly consumed by Reactions 64 and 65. However the small amount of $OH^-(\chi)$ that is produced by Reaction 63, but not consumed by Reactions 64 and 65, is diffusively transported on the YSZ surface. The diffusive molar flux of $OH^-(\chi)$ from TPB is 9.482×10^{-16} mol/cm s. As $OH^-(\chi)$ diffuses away from the TPB on the YSZ surface it is desorbed via Reactions 38 and 41. The reaction-diffusion process causes the spatial profile of $OH^-(\chi)$. The spatial variation in $OH^-(\chi)$ causes a gradient in the $H^-(Zr)$ profile as a result of Reaction 41. However, the magnitude of the $H^-(Zr)$ coverage is very low and it plays a negligible role in the net charge-transfer process.

At a relatively high anode overpotential of $\eta = 0.4$ V ($i = 3.74$ mA/cm^2), the $O^{2-}(\chi)$ consumption rate by the charge-transfer chemistry at the TPB increases to 3.459×10^{-11} mol/cm s. The rate at which $O^{2-}(\chi)$ is supplied to the TPB via surface diffusion is greatly smaller at 1.524×10^{-13} mol/cm s. As in the low current case, the $O^{2-}(\chi)$ is supplied to the TPB region primarily from the bulk via Reaction 35. At higher current density, as a net result of the charge-transfer reactions, the $OH^-(\chi)$ coverage is higher near the TPB and the $OH^-(\chi)$ gradient is larger than in the low current case. However, far from the TPB, the $OH^-(\chi)$ coverage asymptotically approaches approximately 3×10^{-4}, which is the result of equilibration between the surface and gas. The asymptotic $OH^-(\chi)$ coverage is essentially independent of the charge transfer.

Figure 15c illustrates the coverage profiles under cathodic polarization of $\eta = -0.4$ V ($i = -0.063$ mA/cm^2). As may be noted from Tafel plots (e.g., Fig. 8), the magnitude of the current density is much lower at $\eta = -0.4$ V than it is at $\eta = +0.4$ V. The $OH^-(\chi)$ is produced by Reactions 64 and 65 and consumed by Reaction 63 while $O^{2-}(\chi)$ is delivered to the bulk YSZ via Reaction 35. The $O^{2-}(\chi)$ mole flux due to charge-transfer processes at TPB is 5.774×10^{-13} mol/cm s, and the $O^{2-}(\chi)$ diffusion flux is 2.311×10^{-15} mol/cm s. A net $OH^-(\chi)$ mole flux of 3.921×10^{-16} mol/cm s is diffusively transported from the YSZ surface to the TPB, which leads to the decrease in $OH^-(\chi)$ coverage at the TPB.

Solution of the reaction-diffusion model reveals that surface diffusion plays only a minor role in the charge-transfer process. The net charge-transfer process is dominated by thermal chemistry and electrochemistry in the very close vicinity of the TPB. The surface coverages at the TPB, which are central to the charge-transfer process, are established by thermal chemistry on the Ni and YSZ surfaces.

Conclusions

A model has been developed to predict the behavior of patterned-anode experiments. It is based upon solving reaction-diffusion equations on both electrode and electrolyte surfaces. The heterogeneous chemistry on the surfaces and the electrochemical charge transfer at the electrode-electrolyte interfaces (i.e., TPBs) are represented entirely in elementary form. This is a significant departure from the traditional fuel-cell modeling that is based upon global reactions and charge transfer represented in Butler–Volmer form. By representing all the chemistry in elementary form there is no need to evaluate a Nernst potential from the gas-phase composition, and activation overpotentials do not need to be explicitly evaluated. The elementary formulation provides some significant advantages. However, accurate predictions of important observables, such as open-circuit potential, depend upon thermodynamic consistency and microscopic reversibility of all reactions. This requirement, in turn, requires quantitative thermodynamic properties for all species involved in all reactions.

The model is applied to assist interpretation of patterned-anode experiments reported by Mizusaki et al.[1] Several alternative charge-transfer pathways are considered. Although there is certainly no guarantee of uniqueness, the process provides significant quantitative insight about the fundamental chemical and transport processes responsible for charge transfer. Some reaction pathways are seen to provide a good quantitative representation of the measured polarization behavior over wide ranges of gas-phase composition and with both anodic and cathodic biases. Other seemingly reasonable reaction mechanisms, which can represent certain aspects of the data well, are not able to represent the entire data set.

Acknowledgments

We gratefully acknowledge insightful discussions with Professor Wolfgang Bessler (University of Heidelberg and DLR, Stuttgart), Professor Olaf Deutschmann (University of Karlesruhe), Professor Greg Jackson (University of Maryland), and Dr. Graham Goldin (Ansys, Inc.) during the course of this research. The effort was supported by a DoD Research Tools Consortium (RTC) program administered by the Office of Naval Research under grant no. N00014-05-1-0339.

California Institute of Technology assisted in meeting the publication costs of this article.

List of Symbols

a_k	activity of species k
$\dot{c}_e$	production rate of electrons at TPB, mol/cm s
$\dot{c}_k$	molar production rates by charge-transfer reactions, mol/cm s
C_{dl}	double-layer capacitance, F
D_k	diffusion coefficients of the surface species, cm^2/s
E_a	electric-potential difference between the anode and electrolyte, V
E_a^{eq}	equilibrium electric-potential difference between the anode and electrolyte, V
E_c	electric-potential difference between the cathode and electrolyte, V
E_{cell}	cell potential, V
E_k	activation energy, J/mol
F	Faraday constant, C/mol
G^o	standard state Gibbs free energy, J/mol
H_a	anode line thickness, cm
H_e	electrolyte thickness, cm
H_k^o	standard-state species enthalpy, J/mol
i	current density, A/cm^2
i_a	anodic current density, A/cm^2
i_c	cathodic current density, A/cm^2
$i_{e,BV}$	charge-transfer rate in Butler–Volmer equation, A/cm^2
i_{ext}	external current per unit area, A/cm^2
i_F	faradaic current per unit area, A/cm^2
$i_{H_2}^*$	parameter in the expression of i_{0,H_2}, A/cm^2
i_{TPB}	faradaic current per unit TPB length, A/cm
i_0	exchange current density, A/cm^2
I	number of reaction steps
k_a	anodic thermal rate constant of charge-transfer reaction
k_c	cathodic thermal rate constant of charge-transfer reaction
K_{eq}	equilibrium constant
L_a	one-half of the anode linewidth, cm
L_e	one-half of the exposed electrolyte width, cm
p	pressure, dyn/cm^2
p^o	standard-state pressure, dyn/cm^2
p_k	species partial pressure, atm
q_a	anodic rate of charge-transfer reactions, mol/cm s
q_c	cathodic rate of charge-transfer reactions, mol/cm s
q_{dl}	double-layer charge at the anode, C/cm^3
$q_{i,a}$	anodic rate of ith charge-transfer reaction, mol/cm s
$q_{i,c}$	cathodic rate of ith charge-transfer reaction, mol/cm s
R	universal gas constant, J/mol K
$\dot{s}_k$	molar production rates by surface reactions, mol/cm^2 s
S_k^o	standard-state species entropy, J/mol K
t	time, s
T	temperature, K
x	spatial coordinate, cm
$[X_k]$	mole concentrations of surface species, mol/cm^2
X_{V_O}	mole fraction of bulk oxygen vacancy

Greek

α_a	anodic symmetric factor in the Butler–Volmer equation

α_c	cathodic symmetric factor in the Butler–Volmer equation
β_a	anodic symmetric factor in a charge-transfer reaction
β_c	cathodic symmetric factor in a charge-transfer reaction
γ	sticking coefficients
Γ	surface site density, mol/cm^2
θ_k	site fractions of surface species
λ_{TPB}	TPB length per unit area, cm^{-1}
μ_k	species chemical potentials, J/mol
μ_k^o	species standard-state chemical potentials, J/mol
ν_{ki}	reaction stoichiometric coefficient
ν_{ei}	stoichiometry for electrons
σ	ionic conductivity of the electrolyte, S/cm
ϕ_a	anode electric potential, V
ϕ_c	cathode electric potential, V
$\phi_{e,a}$	electrolyte electric potential at anode interface, V
$\phi_{e,c}$	electrolyte electric potential at cathode interface, V
ω	frequency of the harmonic function, Hz

References

1. J. Mizusaki, H. Tagawa, T. Saito, T. Yamamura, K. Kamitani, K. Hirano, S. Ehara, T. Takagi, T. Hikita, M. Ippommatsu, et al., *Solid State Ionics*, **70/71**, 52 (1994).
2. J. Mizusaki, H. Tagawa, T. Saito, K. Kamitani, T. Yamamura, K. Hirano, S. Ehara, T. Takagi, T. Hikita, M. Ippommatsu, et al., *J. Electrochem. Soc.*, **141**, 2129 (1994).
3. B. de Boer, Ph.D. Thesis, University of Twente, Twente, The Netherlands (1998).
4. A. Bieberle and L. J. Gauckler, *Solid State Ionics*, **135**, 337 (2000).
5. A. Bieberle, L. P. Meier, and L. J. Gauckler, *J. Electrochem. Soc.*, **148**, A646 (2001).
6. R. Radhakrishnan, A. V. Virkar, and S. C. Singhal, *J. Electrochem. Soc.*, **152**, A927 (2005).
7. A. M. Sukeshini, B. Habibzadeh, B. P. Becker, C. A. Stoltz, B. W. Eichhorn, and G. S. Jackson, *J. Electrochem. Soc.*, **153**, A705 (2006).
8. R. E. Williford and L. A. Chick, *Surf. Sci.*, **547**, 421 (2003).
9. A. Bieberle and L. J. Gauckler, *Solid State Ionics*, **146**, 23 (2002).
10. M. Mogensen, K. V. Jensen, M. J. Jorgensen, and S. Primdahl, *Solid State Ionics*, **150**, 123 (2002).
11. S. Primdahl and M. Mogensen, *J. Electrochem. Soc.*, **144**, 3409 (1997).
12. P. Holtappels, L. G. J. de Haart, and U. Stimming, *J. Electrochem. Soc.*, **146**, 1620 (1999).
13. P. Holtappels, L. G. J. de Haart, and U. Stimming, *J. Electrochem. Soc.*, **146**, 2976 (1999).
14. D. G. Goodwin, in *Solid Oxide Fuel Cells IX*, S. Singhal and J. Mizusaki, Editors, PV 2005–07, p. 699, The Electrochemical Society Proceedings Series, Pennington, NJ (2005).
15. H. Zhu, R. J. Kee, V. M. Janardhanan, O. Deutschmann, and D. G. Goodwin, *J. Electrochem. Soc.*, **152**, A2427 (2005).
16. R. J. Kee, H. Zhu, and D. G. Goodwin, *Proc. Combust. Inst.*, **30**, 2379 (2005).
17. W. G. Bessler, J. Warnatz, and D. G. Goodwin, *Solid State Ionics*, **177**, 3371 (2007).
18. W. G. Bessler, S. Gewies, and M. Vogler, *Electrochim. Acta*, **53**, 1782 (2007).
19. S. C. DeCaluwe, H. Zhu, R. J. Kee, and G. S. Jackson, *J. Electrochem. Soc.*, **155**, B538 (2008).
20. M. Vogler, A. Bieberle-Hütter, L. Gauckler, J. Warnatz, and W. G. Bessler, *J. Electrochem. Soc.*, **156**, B663 (2009).
21. R. J. Kee, M. E. Coltrin, and P. Glarborg, *Chemically Reacting Flow: Theory and Practice*, John Wiley & Sons, Hoboken, NJ (2003).
22. H. Zhu and R. J. Kee, *J. Electrochem. Soc.*, **155**, B715 (2008).
23. V. M. Janardhanan and O. Deutschmann, *J. Power Sources*, **162**, 1192 (2006).
24. E. S. Hecht, G. K. Gupta, H. Zhu, A. M. Dean, R. J. Kee, L. Maier, and O. Deutschmann, *Appl. Catal., A*, **295**, 40 (2005).
25. M. Mogensen and S. Skaarup, *Solid State Ionics*, **86–88**, 1151 (1996).
26. C. Sun and U. Stimming, *J. Power Sources*, **171**, 247 (2007).
27. M. G. H. M. Hendriks, J. E. ten Elshof, H. J. M. Bouwmeester, and H. Verweij, *Solid State Ionics*, **154–155**, 467 (2002).
28. R. G. Green, L. Barre, and J. B. Giorgi, *Surf. Sci.*, **601**, 792 (2007).
29. T. Nishimura, H. Toi, Y. Hoshino, E. Toyoda, and Y. Kido, *Phys. Rev. B*, **64**, 073404 (2001).
30. K. V. Hansen, K. Norrman, and M. Mogensen, *Surf. Interface Anal.*, **38**, 911 (2006).
31. G. Ballabio, M. Bernasconi, F. Pietrucci, and S. Serra, *Phys. Rev. B*, **70**, 075417 (2004).
32. S. Raz, K. Sasaki, J. Maier, and I. Riess, *Solid State Ionics*, **143**, 181 (2001).
33. A. B. Anderson and E. Vayner, *Solid State Ionics*, **177**, 1355 (2006).
34. A. Hofmann, S. J. Clark, M. Oppel, and I. Hahndorf, *Phys. Chem. Chem. Phys.*, **4**, 3500 (2002).
35. J. A. Kilner, *Solid State Ionics*, **129**, 13 (2000).
36. K. Sasaki and J. Maier, *Solid State Ionics*, **134**, 303 (2000).
37. D. Martin and D. Duprez, *J. Phys. Chem.*, **100**, 9427 (1996).
38. F. Dong, A. Suda, T. Tanabe, Y. Nagai, H. Sobukawa, H. Shinjoh, M. Sugiura, C. Descorme, and D. Duprez, *Catal. Today*, **93–95**, 827 (2004).
39. D. Martin and D. Duprez, *J. Phys. Chem.*, **101**, 4428 (1997).
40. K. D. Jung and A. T. Bell, *Solid State Ionics*, **193**, 207 (2000).
41. S. Cohen and A. Hindmarsh, *Comput. Phys.*, **10**, 138 (1996).
42. P. Deuflhard, E. Hairer, and J. Zugck, *Numer. Math.*, **51**, 501 (1987).
43. J. F. Grcar, R. J. Kee, M. D. Smooke, and J. A. Miller, *Sym. (Int.) Combust., [Proc.]*, **21**, 1773 (1986).
44. D. G. Goodwin, in *Chemical Vapor Deposition XVI and EUROCVD 14*, M. Allendorf, F. Maury, and F. Teyssandier, Editors, PV 2003-08, p. 155, The Electrochemical Society Proceeding Series, Pennington, NJ (2003).
45. W. Bessler, *Solid State Ionics*, **176**, 997 (2005).